Sensitivity of cloud phase distribution to cloud microphysics and thermodynamics in simulated deep convective clouds and SEVIRI retrievals

Cunbo Han[1,2], Corinna Hoose[1], Martin Stengel[3], Quentin Coopman[4], Andrew Barrett[1]

1. Institute of Meteorology and Climate Research (IMK-TRO), Karlsruhe Institute of Technology, Karlsruhe, Germany
2. State Key Laboratory of Tibetan Plateau Earth System, Environment and Resources (TPESER), Institute of Tibetan Plateau Research, Chinese Academy of Sciences, Beijing, China
3. Deutscher Wetterdienst (DWD), Offenbach, Germany
4. Department of Atmospheric and Oceanic Sciences, McGill University, Montreal, Canada

Correspondence to: Cunbo Han (cunbo.han@hotmail.com) and Corinna Hoose (corinna.hoose@kit.edu)

Abstract:

The formation of ice in clouds is an important process in mixed-phase clouds, and the radiative properties and dynamical developments of clouds strongly depend on their partitioning between liquid and ice phases. In this study, we investigated the sensitivities of the cloud phase to ice-nucleating particle (INP) concentration and thermodynamics. Moreover, passive satellite retrieval algorithms and cloud products were evaluated to identify whether they can detect cloud microphysical and thermodynamical perturbations. Experiments were conducted using the ICOsahedral Nonhydrostatic model (ICON) at the convection-permitting resolution of about 1.2 km on a domain covering significant parts of central Europe, and were compared to two different retrieval products based on SEVIRI measurements. We selected a day with multiple isolated deep convective clouds, reaching a homogeneous freezing temperature at the cloud top. The simulated cloud liquid pixel fractions were found to decrease with increasing INP concentration both within clouds and at the cloud top. The decrease in cloud liquid pixel fraction was not monotonic but was stronger in high INP cases. Cloud-top glaciation temperatures shifted toward warmer temperatures with increasing INP concentration by as much as 8 °C. Moreover, the impact of INP concentration on cloud phase partitioning was more pronounced at the cloud top than within the cloud. Moreover, initial and lateral boundary temperature fields were perturbed with increasing and decreasing temperature increments from 0 to +/-3K and +/-5K between 3 and 12 km. Perturbing the initial thermodynamic state was also found to affect the cloud phase distribution systematically. However, the simulated cloud-top liquid pixel fraction, diagnosed using radiative transfer simulations as input to a satellite forward operator and two different satellite remote sensing retrieval algorithms, deviated from one of the satellite products regardless of perturbations in the INP concentration or the initial thermodynamic state for warmer sub-zero temperatures, while agreeing with the other retrieval scheme much better, in particular for the high INP and high convective available potential energy (CAPE) scenarios. Perturbing the initial thermodynamic state, which artificially increases the instability of the mid- and upper-troposphere, brought the simulated cloud-top liquid pixel fraction closer to the satellite observations, especially in the warmer mixed-phase temperature range.

Keywords: Mixed-phase clouds, deep convection, INP, thermodynamics, satellite forward operator, remote-sensing retrieval algorithms

Key points:

1. Cloud properties are retrieved using a satellite forward operator and remote sensing retrieval algorithms with ICON simulations as input. To our knowledge, it is the first time this approach has been used to retrieve cloud phase and other microphysical variables.
2. Glaciation temperature shifts towards a warmer temperature with increasing INP concentration both within the cloud and at the cloud top. Initial thermodynamic states affect the cloud phase distribution significantly as well.
3. Simulated cloud-top liquid pixel fraction matches the satellite observations in the high INP and high CAPE scenarios.

1. Introduction

In the temperature range between 0 and -38°C, ice particles and supercooled liquid droplets can coexist in mixed-phase clouds. Mixed-phase clouds are ubiquitous in Earth's atmosphere, occurring at all latitudes from the poles to the tropics. Because of their widespread nature, mixed-phase processes play a critical role in the life cycle of clouds, precipitation formation, cloud electrification, and the radiative energy balance on both regional and global scales (Korolev et al., 2017). Deep convective clouds are always mixed-phase clouds, and their cloud tops reach the homogeneous freezing temperature, -38°C, in most cases. Despite the importance of mixed-phase clouds in shaping global weather and climate, microphysical processes for mixed-phase cloud formation and development are still poorly understood, especially ice formation processes. It is not surprising that the representation of mixed-phase clouds is one of the big challenges in weather and climate models (McCoy et al., 2016; Korolev et al., 2017; Hoose et al., 2018; Takeishi and Storelvmo, 2018; Vignon et al., 2021; Zhao et al., 2021).

The distribution of cloud phase has been found to impact cloud thermodynamics and Earth's radiation budget significantly (Korolev et al., 2017; Matus and L'Ecuyer, 2017; Hawker et al., 2021). The freezing of liquid droplets releases latent heat and hence affects the thermodynamic state of clouds. Moreover, distinct optical properties of liquid droplets and ice particles exert different impacts on cloud's shortwave and longwave radiation. Simulation and observation studies reported that the cloud phase in the mixed-phase temperature range of convective clouds is influenced by aerosol and plays a significant role in the development into deeper convective systems (Li et al., 2013; Sheffield et al., 2015; Mecikalski et al., 2016). Observational studies reveal that the cloud phase distribution is highly temperature-dependent and influenced by multiple factors, for example, cloud type and cloud microphysics (Rosenfeld et al., 2011; Coopman et al., 2020). Analyzing passive satellite observations of mixed-phase clouds over the Southern Ocean, Coopman et al. (2021) found that cloud ice fraction increases with increasing cloud effective radius. Analysis of both passive and active satellite datasets reveals an increase in supercooled liquid fraction with cloud optical thickness (Bruno et al., 2021).

A number of in-situ observations of mixed-phase clouds have been made in the past several decades, covering stratiform clouds (Pinto, 1998; Korolev and Isaac, 2006; Noh et al., 2013) and convective clouds (Rosenfeld and Woodley, 2000; Stith et al., 2004; Taylor et al., 2016). Aircraft-based observations of mixed-phase clouds properties reveal that the frequency distribution of the ice water fraction has a U-shape with two explicit maxima, one for ice water fraction smaller than 0.1 and the other for ice water fraction larger than 0.9, and the frequency of occurrence of mixed-phase clouds is approximately constant when the ice water fraction is in the range between 0.2 and 0.5 (Korolev et al., 2003; Field et al., 2004; Korolev et al., 2017). These findings are very useful constraints of numerical models (Lohmann and Hoose, 2009; Grabowski et al., 2019). However, in-situ observations of mixed-phase cloud microphysics are technically difficult and sparse in terms of spatial and temporal coverage. Thus, understanding ice formation processes and determining the climatological significance of mixed-phase clouds have proved difficult using existing in-situ observations only.

Both observations and simulations reveal that ice-nucleating particles (INPs) impact deep convective cloud properties including the persistence of deep convective clouds and precipitation (Twohy, 2015; Fan et al., 2016). However, the impact of INPs on precipitation from deep convective clouds is still uncertain and may depend on precipitation and cloud types (van den Heever et al., 2006; Min et al., 2009; Fan et al., 2010; Li and Min, 2010). Although the effects of INPs on convective precipitation are not conclusive, it is certain that the interactions between convective clouds and INPs affect cloud microphysical properties and hence cloud phase distributions. In addition, previous numerical modeling studies on cloud-aerosols interactions have focused on influences of aerosols acting as cloud condensation nuclei (CCN) (Fan et al., 2016), which are linked to the ice phase e.g. through impacts on the riming efficiency (Barrett and Hoose, 2023). Given the limited knowledge on ice formation in deep convective clouds and significant uncertainties in ice nucleation parameterizations, it is necessary to conduct sensitivity simulations to investigate how ice formation processes are influenced by INP concentrations and thermodynamic states in deep convective clouds.

In this study, with the help of realistic convection-permitting simulations using two-moment microphysics, we address how and to what extent INP concentration and thermodynamic state affect the in-cloud and cloud-top phase distributions in deep convective clouds. In particular, cloud properties are retrieved using a satellite forward operator and remote sensing retrieval algorithms with radiative transfer simulations as input for a fair comparison to observations from SEVIRI. This method allows us to compare model simulated cloud properties with remote sensing cloud products directly, and is, to our knowledge, the first time this approach is used for the cloud phase and related microphysical variables. We aim to evaluate the satellite retrieval algorithms and investigate whether passive satellite cloud products can detect cloud microphysical and thermodynamical perturbations.

This paper is structured as follows: In section 2, we introduce our model setups and the experiment design, the satellite forward operator, remote sensing retrieval algorithms, and datasets. Simulation results for the sensitivity experiments are shown in section 3. Section 4 presents discussions; and we summarize the study and draw conclusions in section 5.

2. Data and Method

2.1. Model description

The Icosahedral Nonhydrostatic (ICON) model (Zängl et al., 2015) is a state-of-the-art unified modeling system offering three physics packages, which are dedicated to numerical weather prediction (NWP), climate simulation, and large-eddy simulation. ICON is a fully compressible model and has been developed collaboratively between the German Weather Service (DWD), Max Planck Institute for Meteorology, German Climate Computing Center (DKRZ), and Karlsruhe Institute of Technology (KIT). In order to maximize the model performance and to remove the singularity at the poles, ICON solves the prognostic variables suggested by Gassmann and Herzog (2008), on an unstructured triangular grid with C-type staggering based on a successive refinement of a spherical icosahedron (Wan et al., 2013). Governing equations are described in Wan et al. (2013) and Zängl et al. (2015). The DWD has operated the ICON model at a spatial resolution of about 13 km on the global scale since January 2015. In the global ICON, the higher-resolution ICON-EU (resolution 7 km) nesting area for Europe has been embedded since July 2015. In this study, ICON-2.6.4 with the NWP physics package is used and initial and lateral boundary conditions are provided by the ICON-EU analyses.

For cloud microphysics, we use an updated version of the two-moment cloud microphysics scheme developed by Seifert and Beheng (2006). The two-moment scheme predicts the number and mass mixing ratios of two liquid (cloud and rain) and four solid (ice, graupel, snow, and hail) hydrometers. The cloud condensation nuclei (CCN) activation is described following the parameterization developed by Hande et al. (2016). Homogeneous freezing, including freezing of liquid water droplets and liquid aerosols, is parametrized according to Kärcher et al. (2006). Heterogeneous ice nucleation, including the immersion and deposition modes, is parameterized as a function of temperature- and ice supersaturation-dependent INP concentration (Hande et al., 2015). The INP concentration due to immersion nucleation is described as the following equation:

$$C_{INP}(T_K) = A \times \exp[-B \times (T_K - T_{\min})^C] \quad (1)$$

where T_k is the ambient temperature in Kelvin; *A*, *B*, and *C* are fitting constants with different values to represent seasonally varying dust INP concentrations. The parameterization for deposition INPs is simply scaled to the diagnosed relative humidity with respect to ice (RH_{ice}):

$$C_{INP}(T_K, RH_{ice}) \approx C_{INP}(T_K) \times DSF(RH_{ice}) \quad (2)$$

$$DSF(RH_{ice}) = a \times \arctan(b \times (RH_{ice} - 100) + c) + d \quad (3)$$

where $C_{INP}(T_K)$ is given by Equation (1); *a*, *b*, c, and *d* are constants. More details are found in Hande et al. (2015).

2.2. Simulation setup and sensitivity experiments

In this study, the setup consists of two different domains with one-way nesting covering a major part of central Europe (Figure 1). The horizontal resolution for the nested domains is halved from 2400 m to 1200 m in the innermost domain, and the time steps for the two domains are 12 s and 6 s, respectively. 150 vertical levels are used, with a grid stretching towards the model top at 21 km. The vertical resolution is the same for all horizontal resolutions and the lowest 1000 m encompass 20 layers.

A 1-D vertical turbulence diffusion and transfer scheme is used for the 2400 m and 1200 m resolutions, referred to as numerical weather prediction (NWP) physics. Deep convection is assumed to be explicitly resolved, while shallow convection is parameterized for both domains. The simulations are initialized at 00:00 UTC on the study day from ICON-EU analyses and integrated for 24 hours. Simulation results were saved every 15 minutes. At the lateral boundaries of the outer domain, the simulation of the model is updated with 3-hourly ICON-EU analyses. The nested domains are coupled online, and the outer domain provides lateral boundary conditions to the inner domain.

In nature, INP concentration varies across multiple orders of magnitude (Hoose and Möhler, 2012; Kanji et al., 2017). Thus, in our sensitivity experiments, heterogeneous ice formation was scaled by multiplying the default INP concentration (Equation (1)) with a factor of 10^{-2}, 10^{-1}, 10^{1}, 10^{2}, 10^{3} for both immersion freezing and deposition ice nucleation. Together with a case with default INP concentration (case CTRL) and one case switching off the secondary-ice production via rime-splintering process (the so called Hallet-Mossop process), 7 cases were created in total to investigate the impact of primary and secondary ice formation on cloud phase distribution in deep convective clouds.

In order to assess the sensitivity of the cloud phase to thermodynamics, initial and lateral boundary temperature fields are modified with increasing and decreasing temperature increments, named experiments INC and DEC, respectively. The temperature increment is linearly increased/decreased with height from 0 K at 3 km to +/-3K and +/-5K at 12 km, creating 4 sensitivity experiments DEC03, DEC05, INC03, and INC05. Above 12 km, the increment is constant up to the model top. Initial temperature profiles are shown in Figure 2. The increasing or decreasing environmental temperature leads to changes in the lapse rate and the stability of the atmosphere, and hence results in decrease or increase in the convective available potential energy (CAPE), respectively (Barthlott and Hoose, 2018). Thus, the CAPE increases monotonically from case INC05 (spatial-averaged CAPE at 9:00 UTC: 413 J kg^{-1}) to case CTRL (724 J kg^{-1}) and finally to DEC05 (1235 J kg^{-1}). Note that the relative humidity increases/decreases with decreasing/increasing temperature as the specific humidity is unperturbed. The perturbations of INP concentration and initial/lateral temperature profiles are motivated by Hoose et al. (2018) and Barthlott and Hoose (2018), respectively. Complementary to these earlier studies, we now investigate an ensemble of several deep convective clouds and focus on influences of INP and thermodynamics on cloud phase distribution. Short descriptions of all sensitivity experiments performed in this study are listed in Table 1.

2.3. Satellite observations and retrieval algorithms

The Spinning Enhanced Visible and Infrared Imager (SEVIRI) is a 12-channel imager on board the geostationary Meteosat Second Generation (MSG) satellites. SEVIRI has one high spatial resolution visible channel (HRV) and 11 spectral channels from 0.6 to 14 μm with a 15 min revisit cycle and a spatial resolution of 3 km at nadir (Schmetz et al., 2002). Based on the spectral measurements of SEVIRI, a cloud property data record, the CLAAS-2 dataset (CLoud property dAtAset using SEVIRI, Edition 2), has been generated in the framework of the EUMETSAT Satellite Application Facility on Climate Monitoring (CM SAF) (Benas et al., 2017). CLAAS-2 is the successor of CLAAS-1 (Stengel et al., 2014), for which retrieval updates have been implemented in the algorithm for the detection of clouds compared to CLAAS-1 (Benas et al., 2017) with the temporal coverage being extended to 2004-2015. Retrieval algorithms for parameters that are important for this study are introduced below. Detailed descriptions for the retrieval algorithms are found in Stengel et al. (2014) and Benas et al. (2017) with the main features being summarized in the following.

The MSGv2012 software package is employed to detect clouds and their vertical placement (Derrien and Le Gléau, 2005; Benas et al., 2017). Multi-spectral threshold tests, which depend on illumination and surface types, among other factors, are performed to detect cloud appearances. Each satellite pixel is assigned to categories of cloud-filled, cloud-free, cloud water contaminated, or snow/ice contaminated. Cloud top pressure (CTP) is retrieved with different approaches using input from SEVIRI channels at 6.2, 7.3, 10.8, 12.0, and 13.4 μm (Menzel et al., 1983; Schmetz et al., 1993; Stengel et al., 2014; Benas et al., 2017). Cloud top height (CTH) and cloud top temperature (CTT) are derived from CTP using ancillary data for temperature and humidity profiles from ERA-Interim (Dee et al., 2011). The cloud top phase (CPH) retrieval is based on a revised version of the multispectral algorithm developed by Pavolonis et al. (2005). Clouds are categorized initially into six types, that are liquid, supercooled, opaque ice, cirrus, overlap, and overshooting. Subsequently, the binary cloud phase (liquid or ice) is generated based on the six categories (Benas et al., 2017). Cloud optical and microphysical properties are retrieved using the Cloud Physical Properties (CPP) algorithm (Roebeling et al., 2006). SEVIRI visible (0.6 μm) and near-infrared (1.6 μm) measurements are used to calculate cloud optical thickness (COT) and cloud particle effective radius (r_e) by applying the Nakajima and King (1990) approach in the CPP algorithm (Stengel et al., 2014; Benas et al., 2017). Liquid water path (LWP) and ice water path (IWP) are then computed as a function of liquid/ice water density, COT, and r_e of cloud water and cloud ice following the scheme developed by Stephens (1978).

In this study we used instantaneous CLAAS-2 data with temporal resolution of 15 minutes and on native SEVIRI projection and resolution. In addition to the CLAAS-2 dataset, the recently developed software suite SEVIRI_ML (Philipp and Stengel (2023) in preparation; code available on Github: https://github.com/danielphilipp/seviri_ml) was applied to the SEVIRI measurements to obtain cloud top phase and cloud top temperature for the selected case. SEVIRI_ML uses a machine learning approach calibrated against Cloud-Aerosol Lidar with Orthogonal Polarization (CALIOP) data. One feature of the SEVIRI_ML is that it also provides pixel-based uncertainties such that values with low reliability can be filtered out. We applied the retrieval algorithms to the model simulations in this study and compared the results to satellite observations. A similar strategy was used by Kay et al. (2018) for the evaluation of precipitation in a climate model with CloudSat observations and termed “scale-aware and definition-aware evaluation”.

2.4. Satellite forward operators

In order to compare simulation results and satellite observations directly, SEVIRI-like spectral reflectance and brightness temperatures are calculated using the radiative transfer model for TOVS (RTTOV, v12.3)(Saunders et al., 2018). RTTOV is a fast radiative transfer model for simulating top-of-atmosphere radiances from passive visible, infrared, and microwave downward-viewing satellite radiometers. It has been widely used in simulating synthetic satellite images and assimilating radiances in numerical models (Saunders et al., 2018; Pscheidt et al., 2019; Senf et al., 2020; Geiss et al., 2021; Rybka et al., 2021).

In this work, ICON simulated surface skin temperature, near-surface pressure, temperature, specific humidity, wind velocity, total liquid water content, total ice water content, and effective radius of cloud liquid and cloud ice are used as input to drive the RTTOV model. Before inputting to the RTTOV model, ICON simulations are remapped onto SEVIRI's full disc coordinate. Brightness temperatures from 8 channels (at 3.9, 6.2, 7.3, 8.7, 9.7, 10.8, 12.0, and 13.4 μm) and reflectance from 3 channels (at 0.6, 0.8, and 1.6 μm) simulated by the RTTOV model are used as input to run the remote sensing retrieval algorithms to derive CLAAS-2-like and SEVIRI_ML-like retrievals, named ICON_RTTOV_CLAAS-2 and ICON_RTTOV_SEVIRI_ML products, respectively.

2.5. Synoptic overview

The day 06 June 2016 was selected to analyze, which was dominated by summertime deep convection located in central Europe. The synoptic forcing was weak on the day, and convection was triggered mainly by local thermal instabilities. The day has been discussed frequently in previous studies in terms of convection triggering, cloud microphysics, and its parameterizations (Keil et al., 2019; Geiss et al., 2021).

3. Results and discussion

Perturbing INP concentration and temperature profiles directly affects microphysical and thermodynamic processes of the developing deep convective clouds, and hence impact in-cloud and cloud-top phase distributions. The following section shows results and discussions on the sensitivities of cloud phase and cloud microphysics to INP concentration and thermodynamic perturbations.

3.1. Spatial distribution of cloud properties

Before analyzing the results of sensitivity experiments, retrieved cloud properties via RTTOV and the CLAAS-2 retrieval scheme for the CTRL case are compared to

CLAAS-2 products. Spatial distributions of derived LWP, IWP, and COT at 13:00 UTC of the CTRL case and CLAAS-2 satellite observation are shown in Figure *3*. Discrepancies are found between ICON simulation and CLAAS-2 satellite observations in terms of spatial coverage and intensity. The ICON simulation overestimates the cloud coverage of low-level liquid clouds compared to CLAAS-2 satellite observations, while LWP derived from the ICON simulation (case CTRL) is smaller and more homogeneously distributed than that from the CLAAS-2 observation (Figure 3a and 3b). The spatial distributions of IWP and COT represent the approximate location and spatial extension of deep convective clouds in this study. The ICON simulation could reproduce cores of deep convective clouds of a number and spacing comparable to observations, while the spatial extension and intensity of individual deep convective clouds are not simulated very well by the ICON model. The ICON simulation underestimates the spatial extension of deep convective clouds but overestimates IWP and COT outside the convective cores compared to the CLAAS-2 observation (Figure *3*c-f).

Overall, the simulated clouds appear to be too homogeneous without sufficient internal structure. Geiss et al. (2021) also reported significant deviations between model simulations and satellite observations. The error sources are manifold and may originate from the model physics as well as from the forward operator and the retrieval algorithm. Geiss et al. (2021) investigated the sensitivity of derived visible and infrared observation equivalents to model physics and operator settings. They found that the uncertainty of the visible forward operator is sufficiently low while infrared channels could bring errors in cloud-top variables. Geiss et al. (2021) concluded that the primary source of deviations is mainly from model physics, especially model assumptions on subgrid-scale clouds. In addition to the subgrid-scale cloud scheme, multiple critical cloud microphysical processes missing from the model, introducing significant uncertainties into the simulation results. For example, entrainment mixing process is not resolved or parameterized in the model, which has essential influences on processes at cloud boundaries and hence the cloud properties (Mellado, 2017). Moreover, secondary ice processes including droplet shattering and collisional breakup due to ice particles collisions are missing, which have significant impacts on the cloud ice microphysics (Sullivan et al., 2018; Sotiropoulou et al., 2021).

3.2. Sensitivity of microphysical properties to INP perturbation

Perturbing INP concentration results in a direct influence on the heterogeneous freezing processes and hence impacts on cloud microphysical properties. Systematic variations have been found in the spatial- and time-averaged profiles of mass mixing ratios of cloud hydrometeors as shown in Figure 4. All profiles discussed here are averaged over cloudy pixels (defined as having a condensed mass of cloud water plus total cloud ice greater than a threshold of 1.0×10^{-5} kg kg^{-1}) and over the time period from 9:00 to 19:00 UTC, when convection was well developed. The mass concentration of ice crystals decreases with increasing INP concentration (Figure 4a). However, the mass concentration of snow, graupel, and rainwater increase with increasing INP concentration, especially in the high INP concentration cases (cases $A\times10^2$ and $A\times10^3$).

In order to further reveal why ice crystal mass concentration decreases with increasing INP concentration, we investigate process rates related to ice particle nucleation and growth. Figure 5 shows spatial- and time-averaged (from 9:00 to 19:00 UTC) profiles of process rates for homogeneous freezing, heterogeneous freezing, secondary ice production via the rime-splintering process, cloud droplets rimed with ice crystals, rain droplets rimed with ice crystals, and collection between ice and ice crystals. Heterogeneous freezing (Figure 5a) includes processes of immersion freezing, deposition ice nucleation, and immersion freezing of liquid aerosols (Kärcher et al., 2006; Hande et al., 2015), see also equations (1) and (2). Process rates of heterogeneous freezing increase significantly with increasing INP concentration compared to the CTRL (Figure 5a). Compensating the change in heterogeneous freezing, process rates of homogeneous freezing decrease significantly with increasing INP concentration (Figure 5b). However, a decrease in INP concentration (compared to the CTRL) does not have a strong influence on the heterogeneous freezing mass rate, which is already low compared to the other processes in CTRL. Riming processes of cloud droplets and rain droplets onto ice crystals are greatly invigorated due to enhanced INP concentration (Figure 5d and 5e). Moreover, process rates of secondary ice production due to rime-splintering are strengthened as well due to the increase in rimed ice, albeit much lower values. Figure 5f shows process rates of collection between ice and ice crystals. Process rates of collection between ice and ice particles increase with increasing INP concentration, especially in high INP concentration cases (cases A$\times$10^2 and A$\times$10^3). Process rates of collection of other ice particles all increase with increasing INP concentration, similar to the collection between ice and ice crystals (not shown). The increase in the riming of clouds and rain droplets onto ice crystals and collections between ice particles leads to the increase in the mass concentration of snow, graupel, and hail (Figure 4b and 4c). However, the total mass increase in snow, graupel, and hail do not outbalance the decrease in the mass concentration of ice crystals (Figure 4). The weakened homogeneous freezing is most likely the dominant factor leading to the decrease in ice mass concentration in high INP cases, considering the magnitude of the process rate of homogeneous freezing (Figure 5b). Supercooled liquid and cloud droplets have been converted into ice crystals before reaching the homogeneous freezing layer, leading to fewer supercooled droplets remaining for homogeneous freezing. Even though homogeneous freezing is weakened in high INP cases, the process rate of homogeneous freezing is still larger than heterogeneous freezing, which means homogeneous freezing is the dominant ice formation process in the convective clouds discussed in this study. Moreover, the enhanced production of large ice particles (snow, graupel, and hail) in the highest INP case, which sediment more rapidly to lower levels, leads to increased surface precipitation by about 10% in the A$\times$10^3 case (not shown). Interestingly, ice crystal effective radius (r_e^{ice}) increases monotonically with increasing INP concentration, especially in the mixed-phase layer (Figure *4*e). Zhao et al. (2019) also reported an increased r_e^{ice} with polluted continental aerosols in their simulated moderate convection cases, and they attributed it to enhanced heterogeneous freezing and prolonged ice crystal growth at higher INP loading.

This competition between homogeneous and heterogeneous freezing has been discussed in previous studies (Heymsfield et al., 2005; Deng et al., 2018; Takeishi and Storelvmo, 2018). In contrast, simulations of mixed-phase moderately deep convective clouds by Miltenberger and Field (2021) indicate that cloud ice mass concentration increases with increasing INP concentration, which is in opposition to the findings in this work. The main reason is that the CTT is about -18°C in Miltenberger and Field (2021)'s study, and heterogeneous freezing does not compete with homogeneous freezing. Thus, results on INPs effects on glaciation processes in convective clouds can be opposite under different conditions.

3.3. Cloud liquid mass fraction

Varying the INP concentration has a direct impact on the primary ice formation. Thus, it affects cloud liquid mass fraction within the clouds (directly for all cloudy layers where heterogeneous freezing is active and indirectly for warmer and colder temperatures) and at the cloud top. Cloud liquid mass fraction is defined as the ratio of mass mixing ratio between cloud droplets (q_c) and the sum of cloud droplets and cloud ice crystals (q_i). In-cloud liquid mass fraction, sampled at a time interval of 15 minutes between 9:00 to 19:00 from all cloudy pixels, is shown as scatterplots versus temperature in Figure 6a-d. The corresponding frequencies of the occurrence of the temperature/liquid fraction bins are shown in Figure 6e-h. Similar analyses were made by Hoose et al. (2018), but for idealized simulations of deep convective clouds. In-cloud liquid mass fractions smaller than 0.5 are quite common already at temperature just below -3 °C except for the case without rime-splintering process (A$\times 10^0$_NSIP). The decrease in INP concentrations has limited effects on the in-cloud liquid mass fraction (Figure 6c and 6g), while a stronger influence has been found in the case with enhanced INP concentration (Figure 6d and 6h). The number of pixels having high liquid mass fraction values at temperatures lower than -30 °C decreases with increasing INP concentration. In addition, more and more pixels having liquid mass fraction smaller than 0.5 appear with increasing INP concentration and the number of pure ice pixels increases with increasing INP concentration as well. This is because higher INP concentration intensifies the heterogeneous freezing processes (immersion freezing and deposition ice nucleation) and invigorates the rime-splintering process as well (will be discussed in section 3.4). Interestingly, at the lower end of the mixed-phase temperature range (-38 ~ -28 °C), there are fewer pixels having high liquid mass fraction in the high INP case, and those remaining are mainly the ones at high vertical velocities (above ~ 10 m/s). This is probably because supercooled droplets are more easily frozen in high INP cases and stronger updrafts are needed to offset the Wegener-Begeron-Findeisen (WBF) process to maintain the supersaturation with respect to water. Switching off the secondary ice production via rime-splintering process, pixels having a liquid mass fraction smaller than 0.9 are reduced significantly at temperatures between -10 °C and 0 °C (Figure 6b and 6f).

At the cloud top (Figure 7), the number of pixels having a liquid mass fraction smaller than 0.5 increases with increasing INP concentration, which is the same as within the clouds. “Cloud top” is defined as the height of the uppermost cloud layer (which has a condensed mass of cloud water plus cloud total cloud ice greater than a threshold of 1.0×10^{-5} kg kg^{-1}) in a pixel column. At the cloud top, the liquid mass fraction has a more polarized distribution, with either large values or small values, and intermediate values are less common than within the clouds. This is because the vertical velocities at the cloud top are significantly smaller compared to that within the cloud, which leads to a more efficient WBF process at the cloud top.

3.4. Liquid cloud pixel fraction

Liquid cloud pixel fractions are calculated differently for model simulations and retrieved cloud products. For simulation results, a cloudy pixel having a cloud liquid mass fraction larger than 0.5 is counted as a liquid pixel, otherwise, it is an ice pixel. Both CLAAS-2 and SEVIRI_ML products and the corresponding retrievals derived from ICON simulations by the satellite forward operators (see section 2.4) provide binary cloud phase information (liquid or ice) only. For these data, the liquid cloud pixel fraction is calculated as the ratio between the number of liquid cloud pixels and the sum of all cloudy pixels.

Liquid cloud pixel fractions within clouds and at the cloud top are shown in Figure 8. Decrease in INP concentration has limited impacts on the liquid cloud pixel fraction for in-cloud layers. Increase in INP concentration leads to a decrease in liquid cloud pixel fraction but not monotonically (Figure 8a). The decrease in liquid cloud pixel fraction is significant in the highest INP concentration case (case $A\times10^3$), while decreases in intermediate INP concentration cases (cases $A\times10^1$ and $A\times10^2$) are only obvious in temperature ranges from -30 °C to -20 °C and from -15 °C to -5 °C. Moreover, liquid mass fraction decreases monotonically with increasing INP concentration in the temperature range from about -15 to -35 ˚C both within the cloud and at the cloud top (except for the lowest INP concentrations), and the decreasing trend is more significant at the cloud top compared to within the cloud (not shown). Switching off the rime-splintering process results in an increase in liquid cloud pixel fraction in the temperature range between -10 °C and -3 °C, which is consistent with the strong decrease in pixels of cloud liquid mass fraction lower than 0.9 in the same temperature range (Figure 7b). The temperature at which the liquid cloud pixel fraction equals 0.5 is often termed “glaciation temperature”. The glaciation temperature shifts slightly to a warmer temperature by ~2 °C at the highest INP concentration case (case $A\times10^3$, Figure *8*a).

Sensitivities of the cloud phase to INP concentration are more complex at the cloud top than inside the cloud. Liquid cloud pixel fractions at the cloud top calculated directly from ICON simulations on its native grid (~1200 m) are shown in Figure 8b. Cloud-top liquid pixel fraction decreases significantly with increasing INP concentration. In the temperature range between -35 °C and -15 °C, where heterogeneous freezing processes (immersion freezing and deposition nucleation) are dominant, the impact of INP is most pronounced. Above -15 °C, the impact of INP does not disappear, especially in the highest INP concentration case (case $A\times10^3$). This is mostly likely due to the sedimentation of ice crystals from upper layers and the secondary ice production invigorated by the WBF process. Switching off the rime-splintering process increases cloud-top liquid pixel fraction only slightly in the temperature range from -10 °C to -3 °C and is almost identical to the control run (case CTRL) outside this temperature range. Interestingly, the shift of glaciation temperature with increasing INP concentration is about 8 °C (Figure 8b) at the cloud top, which is stronger than that inside the clouds (~2 °C, Figure 8a). A possible explanation is that, typically, the vertical velocity at the cloud top is smaller than within the cloud and the ice formation through the WBF process is expected to be more efficient. Thus, the WBF process is more sensitive to INP perturbation at the cloud top than within clouds, and leads to the glaciation temperature shifting to be more significant at the cloud top.

Liquid cloud pixel fractions at the cloud top calculated directly from ICON simulations on SEVIRI’s grid (~ 5000 m) are shown in Figure 8c. They are noisier and do not exhibit the small minimum between -10 °C and -3 °C related to rime-splintering, but are otherwise very similar to Figure 8b. In contrast, the scale-aware and definition-aware ICON_RTTOV_CLAAS-2 cloud-top liquid pixel fractions shown in Figure 8d differ markedly from the direct or regridded model output. Above -23 °C, increase and decrease in INP concentration both lead to a decrease in cloud-top liquid pixel fraction at certain temperature, but the high INP concentration cases (cases $A\times10^2$ and $A\times10^3$), still exhibit the lowest liquid fractions, and case $A\times10^0$_NSIP the highest. Thus, the fingerprints of primary and secondary ice formation are retained in the ICON_RTTOV_CLAAS-2 liquid fraction in this temperature range only for very strong perturbations. At the same time, it must be noted that the decrease of the liquid pixel fraction to values around 0.8 above -15 °C is not related to the rime-splintering process, but to the application of the CLAAS-2 satellite simulator. Below -23 °C, in the high INP cases $A\times10^2$ and $A\times10^3$, cloud-top liquid pixel fractions even increase with increasing INP concentration. In moderate and low INP cases, the impacts of INP perturbation are not pronounced. Moreover, the shape of cloud-top liquid pixel fraction decreasing with cloud-top temperature is different from that in Figure 8b. Here, the fingerprints of the ice formation processes are completely lost. As demonstrated in Figure 8c, remapping of simulation data onto SEVIRI's coarser grid is not the cause of liquid pixel fraction difference between direct ICON output and the ICON_RTTOV_CLAAS-2 diagnostics, but the CLAAS-2 retrieval algorithm itself is responsible.

The satellite observed cloud-top liquid pixel fraction from CLAAS-2 is plotted as a grey dashed line in Figure 8d. It does not reach 1.0 for all cases even as the cloud-top temperature is approaching 0 °C, and shows a different temperature dependency than the simulated curves. No matter how strong the INP concentration and rime-splintering are perturbed, the retrieved cloud-top liquid pixel fractions from simulation data deviate strongly from the CLAAS-2 products. In this context one should note that in particular cloud edges have been found to be problematic situations for the cloud retrievals, being to some extent responsible for biasing the liquid-pixel fraction towards smaller values, in particular for the CLAAS-2 data.

Finally, the comparison to observations is repeated with the SEVIRI_ML retrieval scheme applied to both simulated radiances (ICON_RTTOV_SEVIRI_ML) and the

SEVIRI observations themselves (Figure 8e). As SEVIRI_ML provides uncertainty estimates, pixels for which either the cloud mask uncertainty or the cloud phase uncertainty is larger than 10% are filtered out. While this ensures that only very certain values are kept, it has a significant impact on the number of remaining values as more than 90% of the pixels are filtered out. The filtering affects pixels rather randomly, thus we could not identify any patterns of pixels, such as cloud edges, that are primarily affected by the filtering. The resulting liquid pixel fractions ICON_RTTOV_SEVIRI_ML bear a much stronger similarity to the regridded model output in Figure 8c. Remaining differences are a noisier behavior, a plateau of non-zero liquid pixel fractions even below -40 °C, and a general shift to lower temperatures. SEVIRI_ML applied to observations (dashed black line in Figure 8e), with the same uncertainty criterion, exhibits the expected behavior with a liquid fraction of approximately 1 above -10 °C and 0 below approximately -30 °C, and results in a very good agreement to the $A\times10^3$ case. Generally, the SEVIRI_ML retrieval algorithm is assumed to perform better than the CLAAS-2 scheme for both cloud top temperature and cloud phase. This is because SEVIRI_ML employs state-of-the-art neural networks to emulate CALIOP v4 data. Moreover, SEVIRI_ML provides uncertainty estimates which facilitates fliting out pixels with high uncertainties. Nevertheless, retrieval inaccuracies are unavoidable for passive satellite retrievals which holds true for CLAAS-2 but also for SEVIRI_ML.

3.5. Sensitivity of cloud phase to atmospheric stability perturbations

In addition to the reference run (case CTRL), four cases with perturbations in initial temperatures are analyzed. Mean updraft velocities increase gradually from the low CAPE case INC05 to high CAPE case DEC05 (Figure 9) and cause differences in cloud microphysics and cloud phase distributions.

In-cloud and cloud-top liquid cloud pixel fractions for the five cases are shown in Figure 10. Systematic shifting of liquid cloud pixel fractions is detected both inside clouds and at the cloud top. Liquid cloud pixel fraction decreases with increasing CAPE from INC05 to DEC05. Both in-cloud and cloud-top glaciation temperatures shift toward warmer temperatures as the CAPE increases from case INC05 to DEC05. This is different from the results reported by Hoose et al. (2018) that cloud-top glaciation temperatures hardly changed with increasing temperature in the boundary-layer by 2 °C, and appears to be contradictory to the expectation that stronger vertical velocities result in a lower glaciation temperature due to suppression of the WBF process (Korolev, 2007). Further analysis (not shown) revealed that the mass concentration of cloud ice particle increases while the mass concentration of cloud droplet decreases with the increase in CAPE from case INC05 to DEC05. Moreover, homogeneous and heterogeneous freezing are both enhanced in the high CAPE cases (Figure *11*), possibly due to more transport of moisture to upper levels in the stronger updrafts (Figure *9*). With more ice generated, the WBF process can be stimulated despite the higher updrafts. Interestingly, cloud-top liquid pixel fractions from the two high CAPE cases (cases DEC03 and DEC05) are closer to SEVIRI observations, both using the CLAAS-2 retrieval (Figure 10c) and the SEVIRI_ML retrieval (Figure 10d), especially in the temperature range between -10 and -28 °C.

Compared to the INP perturbation, the impact of thermodynamical perturbation on cloud phase distribution is significantly stronger within the cloud (Figure *8*a and Figure *10*a). At the cloud top, the effect of perturbation in thermodynamics on the cloud phase distribution is as large as the largest INP perturbation (case $A \times 10^3$). Moreover, the impacts of thermodynamical perturbation on domain-averaged profiles of cloud hydrometeors and process rates related to the ice cloud process are also significantly stronger than the INP perturbation. Thus, the thermodynamical perturbation is stronger than the INP perturbation when the entire depth of the cloud is considered. Overall, perturbing initial thermodynamic states or CAPE of convective clouds is as important as and may even stronger than the modifications to cloud heterogeneous freezing parameterizations.

4. Conclusions

Remote sensing products, which cover the entire globe, provide a unique opportunity to constrain the representation of cloud microphysics in global and regional numerical models. In this study, instead of comparing simulation results to satellite observations directly, we derived cloud properties using a radiative transfer model and two different satellite remote sensing retrieval algorithms and then performed the comparison. This enables us to make apples-to-apples comparisons between model simulations and satellite observations. A series of numerical experiments were performed applying convection-permitting simulations with perturbations in INP concentrations and initial thermodynamic states to investigate their impacts on cloud phase distributions in deep convective clouds. Moreover, cloud properties were derived using a satellite forward operator and retrieval algorithms with ICON simulations as input, and compared with CLAAS-2 and SEVIRI_ML satellite cloud products to evaluate whether satellite retrievals could detect perturbations in cloud microphysics and thermodynamics. Uncertainties in the forward operator were however not assessed in this study, which may influence the validity of corresponding results in some extent.

INP concentration was found to have a significant role in shaping cloud phase distributions both within clouds and at the cloud top. Cloud liquid pixel fraction decreased with increasing INP concentration both within the cloud and at the cloud top, indicating a higher glaciation temperature and more intense heterogeneous freezing processes in enhanced INP concentration cases. Interestingly, the influences of INP did not increase linearly but are more pronounced in the high INP concentration cases. In addition, the shifting of glaciation temperature was more significant at the cloud top than within the cloud, which means the impact of INP concentration on cloud phase distribution is more pronounced at the cloud top. It turned out that with the CLAAS-2 retrieval scheme, the INP sensitivity of the cloud-top phase distribution was not detectable, while the SEVIRI_ML retrieval scheme, for which the most uncertain pixels could be excluded, resulted in a better agreement and retained the sensitivity to INP. In contrast, secondary ice production via rime-splintering did not have a detectable impact on the cloud-top phase distribution. Therefore, in future studies, we recommend using the SEVIRI_ML retrieval scheme and SEVIRI_ML satellite-based cloud products.

Ice crystal mass concentration did not increase but decreases with increasing INP concentrations in the simulated deep convective clouds. Process rate analyses revealed that heterogeneous freezing process rates increased with increasing INP concentration, while homogeneous freezing process rates decreased with increasing INP concentration. The competition between heterogeneous freezing and homogeneous freezing for water vapor suppressed ice formation via homogeneous freezing, which was the dominant nucleation process in the simulated deep convective clouds, and hence reduced the cloud ice mass concentration. The increase in heterogeneous nucleation in high INP cases invigorated riming and collection processes of ice particles, making it easier for small ice crystals to grow into large ice aggregates and sediment to lower levels. This was the reason why precipitation increases in enhanced INP cases.

Perturbations in initial thermodynamic states had a strong impact on the cloud phase distribution both within the cloud and at the cloud top, although the used perturbations might be rather large compared to initial condition uncertainty in a weather forecasting context. Moreover, cloud thermodynamics can perturb the cloud phase distribution even stronger than microphysics. To completely distinguish microphysical impacts from thermodynamic impacts, applying a piggybacking approach (Grabowski, 2015; Thomas et al., 2023) in future simulations is necessary.

Utilizing satellite forward operator (the RTTOV radiative model) and remote sensing retrieval algorithms enabled us to derive cloud-top microphysical properties and compare simulation results to satellite products more consistently. However, there were significant differences in retrieved cloud-top liquid fractions between model simulations and satellite products. The sources of errors were very complicated and may come from simulation results, satellite operators, and retrieval algorithms, which will be investigated in the future. Moreover, the cloud-top property analysis presented in this study was based on domain-wide statistics, including clouds of varying types. Statistical results could differ if individual clouds are tracked, as clouds differ in different experiments in terms of locations and extensions. Although there are significant uncertainties in satellite forward operators and retrieval algorithms, passively remote-sensed cloud products provide potential opportunities to constrain microphysical processes in numerical models.

Simulation results of this study revealed a close dependence of heterogeneous freezing and cloud phase distribution on INP concentrations. Despite this finding, the ice formation processes in deep convective clouds remain poorly understood. It is necessary to investigate how and in which conditions the competition of heterogeneous with homogeneous freezing for water vapor and cloud water depends on INP availability and vertical velocities in different types of deep convective clouds. Moreover, the importance of other secondary ice production processes than rime-splintering (droplet shattering and collisional breakup) in deep convective clouds need to be quantified in the future.

Code/Data availability

The codes and data support the findings of this study are available from the corresponding author upon reasonable request.

Author contribution

Corinna Hoose and Cunbo Han conceptualized the study, Cunbo Han did the ICON simulation, ran the RTTOV model, and analyzed the results, Martin Stengel ran the retrieval algorithms and analyzed the results. Cunbo Han wrote the paper with support from all co-authors. Cunbo Han and Corinna Hoose oversaw the review process.

Competing interests

One of the (co-)authors (Corinna Hoose) is a member of the editorial board of Atmospheric Chemistry and Physics.

Acknowledgments

This project has received funding from the European Research Council (ERC) under the European Union's Horizon 2020 research and innovation programme under grant agreement 714062 (ERC Starting Grant “C2Phase”). We gratefully acknowledge the computing time allowed by the German Climate Computing Centre (DKRZ) on the HPC system Mistral and the Steinbuch Centre for Computing (SCC) on the HPC system ForHLR II. The contribution of Martin Stengel was supported by EUMETSAT and its member states through CM SAF.

References

Barrett, A. I. and Hoose, C.: Microphysical pathways active within thunderstorms and their sensitivity to CCN concentration and wind shear, Journal of Geophysical Research: Atmospheres, 128, e2022JD036965, https://doi.org/10.1029/2022JD036965, 2023.

Barthlott, C. and Hoose, C.: Aerosol effects on clouds and precipitation over central Europe in different weather regimes, Journal of the Atmospheric Sciences, 75, 4247-4264, https://doi.org/10.1175/JAS-D-18-0110.1, 2018.

Benas, N., Finkensieper, S., Stengel, M., van Zadelhoff, G. J., Hanschmann, T., Hollmann, R., and Meirink, J. F.: The MSG-SEVIRI-based cloud property data record CLAAS-2, Earth Syst. Sci. Data, 9, 415-434, http://dx.doi.org/10.5194/essd-9-415-2017, 2017.

Bruno, O., Hoose, C., Storelvmo, T., Coopman, Q., and Stengel, M.: Exploring the cloud top phase partitioning in different cloud types using active and passive satellite sensors, Geophysical Research Letters, 48, e2020GL089863-e082020GL089863, https://doi.org/10.1029/2020GL089863, 2021.

Coopman, Q., Hoose, C., and Stengel, M.: Analysis of the thermodynamic phase transition of tracked convective clouds based on geostationary satellite observations, Journal of Geophysical Research: Atmospheres, 125, e2019JD032146, https://doi.org/10.1029/2019JD032146, 2020.

Coopman, Q., Hoose, C., and Stengel, M.: Analyzing the thermodynamic phase partitioning of mixed phase clouds over the southern ocean using passive satellite observations, Geophysical Research Letters, 48, e2021GL093225, https://doi.org/10.1029/2021GL093225, 2021.

Dee, D. P., Uppala, S. M., Simmons, A. J., Berrisford, P., Poli, P., Kobayashi, S., Andrae, U., Balmaseda, M. A., Balsamo, G., Bauer, P., Bechtold, P., Beljaars, A. C. M., van de Berg, L., Bidlot, J., Bormann, N., Delsol, C., Dragani, R., Fuentes, M., Geer, A. J., Haimberger, L., Healy, S. B., Hersbach, H., Hólm, E. V., Isaksen, L., Kållberg, P., Köhler, M., Matricardi, M., McNally, A. P., Monge-Sanz, B. M., Morcrette, J. J., Park, B. K., Peubey, C., de Rosnay, P., Tavolato, C., Thépaut, J. N., and Vitart, F.: The ERA-Interim reanalysis: configuration and performance of the data assimilation system, Quarterly Journal of the Royal Meteorological Society, 137, 553-597, https://doi.org/10.1002/qj.828, 2011.

Deng, X., Xue, H., and Meng, Z.: The effect of ice nuclei on a deep convective cloud in South China, Atmospheric Research, 206, 1-12, https://doi.org/10.1016/j.atmosres.2018.02.013, 2018.

Derrien, M. and Le Gléau, H.: MSG/SEVIRI cloud mask and type from SAFNWC, International Journal of Remote Sensing, 26, 4707-4732, https://doi.org/10.1080/01431160500166128, 2005.

Fan, J., Comstock, J. M., and Ovchinnikov, M.: The cloud condensation nuclei and ice nuclei effects on tropical anvil characteristics and water vapor of the tropical tropopause layer, Environmental Research Letters, 5, 044005, https://doi.org/10.1088/1748-9326/5/4/044005, 2010.

Fan, J., Wang, Y., Rosenfeld, D., and Liu, X.: Review of aerosol–cloud interactions: Mechanisms, significance, and challenges, Journal of the Atmospheric Sciences, 73, 4221-4252, https://doi.org/10.1175/JAS-D-16-0037.1, 2016.

Field, P. R., Hogan, R. J., Brown, P. R. A., Illingworth, A. J., Choularton, T. W., Kaye, P. H., Hirst, E., and Greenaway, R.: Simultaneous radar and aircraft

observations of mixed-phase cloud at the 100 m scale, Quarterly Journal of the Royal Meteorological Society, 130, 1877-1904, https://doi.org/10.1256/qj.03.102, 2004.
Gassmann, A. and Herzog, H.-J.: Towards a consistent numerical compressible non-hydrostatic model using generalized Hamiltonian tools, Quarterly Journal of the Royal Meteorological Society, 134, 1597-1613, http://dx.doi.org/10.1002/qj.297, 2008.
Geiss, S., Scheck, L., de Lozar, A., and Weissmann, M.: Understanding the model representation of clouds based on visible and infrared satellite observations, Atmos. Chem. Phys., 21, 12273-12290, https://doi.org/10.5194/acp-21-12273-2021, 2021.
Grabowski, W. W.: Untangling microphysical impacts on deep convection applying a novel modeling methodology, Journal of the Atmospheric Sciences, 72, 2446-2464, https://doi.org/10.1175/JAS-D-14-0307.1, 2015.
Grabowski, W. W., Morrison, H., Shima, S.-I., Abade, G. C., Dziekan, P., and Pawlowska, H.: Modeling of cloud microphysics: Can we do better?, Bulletin of the American Meteorological Society, 100, 655-672, https://doi.org/10.1175/BAMS-D-18-0005.1, 2019.
Hande, L. B., Engler, C., Hoose, C., and Tegen, I.: Seasonal variability of Saharan desert dust and ice nucleating particles over Europe, Atmos. Chem. Phys., 15, 4389-4397, http://dx.doi.org/10.5194/acp-15-4389-2015, 2015.
Hande, L. B., Engler, C., Hoose, C., and Tegen, I.: Parameterizing cloud condensation nuclei concentrations during HOPE, Atmos. Chem. Phys., 16, 12059-12079, http://dx.doi.org/10.5194/acp-16-12059-2016, 2016.
Hawker, R. E., Miltenberger, A. K., Wilkinson, J. M., Hill, A. A., Shipway, B. J., Cui, Z., Cotton, R. J., Carslaw, K. S., Field, P. R., and Murray, B. J.: The temperature dependence of ice-nucleating particle concentrations affects the radiative properties of tropical convective cloud systems, Atmos. Chem. Phys., 21, 5439-5461, https://doi.org/10.5194/acp-21-5439-2021, 2021.
Heymsfield, A. J., Miloshevich, L. M., Schmitt, C., Bansemer, A., Twohy, C., Poellot, M. R., Fridlind, A., and Gerber, H.: Homogeneous ice nucleation in subtropical and tropical convection and its influence on cirrus anvil microphysics, Journal of the Atmospheric Sciences, 62, 41-64, http://dx.doi.org/10.1175/JAS-3360.1, 2005.
Hoose, C. and Möhler, O.: Heterogeneous ice nucleation on atmospheric aerosols: a review of results from laboratory experiments, Atmos. Chem. Phys., 12, 9817-9854, https://doi.org/10.5194/acp-12-9817-2012, 2012.
Hoose, C., Karrer, M., and Barthlott, C.: Cloud top phase distributions of simulated deep convective clouds, Journal of Geophysical Research: Atmospheres, 123, 10,410-464,476, https://doi.org/10.1029/2018JD028381, 2018.
Kanji, Z. A., Ladino, L. A., Wex, H., Boose, Y., Burkert-Kohn, M., Cziczo, D. J., and Krämer, M.: Overview of ice nucleating particles, Meteorological Monographs, 58, 1.1-1.33, https://doi.org/10.1175/AMSMONOGRAPHS-D-16-0006.1, 2017.
Kärcher, B., Hendricks, J., and Lohmann, U.: Physically based parameterization of cirrus cloud formation for use in global atmospheric models, Journal of Geophysical Research: Atmospheres, 111, https://doi.org/10.1029/2005JD006219, 2006.
Kay, J. E., L'Ecuyer, T., Pendergrass, A., Chepfer, H., Guzman, R., and Yettella, V.: Scale-aware and definition-aware evaluation of modeled near-surface precipitation frequency using CloudSat observations, Journal of Geophysical

Research: Atmospheres, 123, 4294-4309, https://doi.org/10.1002/2017JD028213, 2018.

Keil, C., Baur, F., Bachmann, K., Rasp, S., Schneider, L., and Barthlott, C.: Relative contribution of soil moisture, boundary-layer and microphysical perturbations on convective predictability in different weather regimes, Quarterly Journal of the Royal Meteorological Society, 145, 3102-3115, https://doi.org/10.1002/qj.3607, 2019.

Korolev, A. and Isaac, G. A.: Relative humidity in liquid, mixed-phase, and ice clouds, Journal of the Atmospheric Sciences, 63, 2865-2880, https://doi.org/10.1175/JAS3784.1, 2006.

Korolev, A.: Limitations of the Wegener–Bergeron–Findeisen mechanism in the evolution of mixed-phase clouds, Journal of the Atmospheric Sciences, 64, 3372-3375, http://dx.doi.org/10.1175/JAS4035.1, 2007.

Korolev, A., McFarquhar, G., Field, P. R., Franklin, C., Lawson, P., Wang, Z., Williams, E., Abel, S. J., Axisa, D., Borrmann, S., Crosier, J., Fugal, J., Krämer, M., Lohmann, U., Schlenczek, O., Schnaiter, M., and Wendisch, M.: Mixed-phase clouds: Progress and challenges, Meteorological Monographs, 58, 5.1-5.50, https://doi.org/10.1175/AMSMONOGRAPHS-D-17-0001.1, 2017.

Korolev, A. V., Isaac, G. A., Cober, S. G., Strapp, J. W., and Hallett, J.: Microphysical characterization of mixed-phase clouds, Quarterly Journal of the Royal Meteorological Society, 129, 39-65, https://doi.org/10.1256/qj.01.204, 2003.

Li, R. and Min, Q. L.: Impacts of mineral dust on the vertical structure of precipitation, Journal of Geophysical Research: Atmospheres, 115, https://doi.org/10.1029/2009JD011925, 2010.

Li, X., Tao, W.-K., Masunaga, H., Masunaga, Gu, G., and Zeng, X.: Aerosol effects on cumulus congestus population over the tropical acific: A cloud-resolving modeling study, Journal of the Meteorological Society of Japan, 91, 817-833, 10.2151/jmsj.2013-607, 2013.

Lohmann, U. and Hoose, C.: Sensitivity studies of different aerosol indirect effects in mixed-phase clouds, Atmos. Chem. Phys., 9, 8917-8934, https://doi.org/10.5194/acp-9-8917-2009, 2009.

Matus, A. V. and L'Ecuyer, T. S.: The role of cloud phase in Earth's radiation budget, Journal of Geophysical Research: Atmospheres, 122, 2559-2578, https://doi.org/10.1002/2016JD025951, 2017.

McCoy, D. T., Tan, I., Hartmann, D. L., Zelinka, M. D., and Storelvmo, T.: On the relationships among cloud cover, mixed-phase partitioning, and planetary albedo in GCMs, Journal of Advances in Modeling Earth Systems, 8, 650-668, https://doi.org/10.1002/2015MS000589, 2016.

Mecikalski, J. R., Jewett, C. P., Apke, J. M., and Carey, L. D.: Analysis of Cumulus Cloud Updrafts as Observed with 1-Min Resolution Super Rapid Scan GOES Imagery, Monthly Weather Review, 144, 811-830, https://doi.org/10.1175/MWR-D-14-00399.1, 2016.

Mellado, J. P.: Cloud-top entrainment in stratocumulus clouds, Annual Review of Fluid Mechanics, 49, 145-169, 10.1146/annurev-fluid-010816-060231, 2017.

Menzel, W. P., Smith, W. L., and Stewart, T. R.: Improved cloud motion wind vector and altitude assignment using VAS, Journal of Applied Meteorology and Climatology, 22, 377-384, https://doi.org/10.1175/1520-0450(1983)022<0377:ICMWVA>2.0.CO;2, 1983.

Miltenberger, A. K. and Field, P. R.: Sensitivity of mixed-phase moderately deep convective clouds to parameterizations of ice formation – an ensemble perspective, Atmos. Chem. Phys., 21, 3627-3642, http://dx.doi.org/10.5194/acp-21-3627-2021, 2021.

Min, Q. L., Li, R., Lin, B., Joseph, E., Wang, S., Hu, Y., Morris, V., and Chang, F.: Evidence of mineral dust altering cloud microphysics and precipitation, Atmospheric Chemistry and Physics, 9, 3223-3231, https://doi.org/10.5194/acp-9-3223-2009, 2009.

Nakajima, T. and King, M. D.: Determination of the optical thickness and effective particle radius of clouds from reflected solar radiation measurements. Part I: Theory, Journal of Atmospheric Sciences, 47, 1878-1893, https://doi.org/10.1175/1520-0469(1990)047<1878:DOTOTA>2.0.CO;2, 1990.

Noh, Y.-J., Seaman, C. J., Vonder Haar, T. H., and Liu, G.: In situ aircraft measurements of the vertical distribution of liquid and ice water content in midlatitude mixed-phase clouds, Journal of Applied Meteorology and Climatology, 52, 269-279, https://doi.org/10.1175/JAMC-D-11-0202.1, 2013.

Pavolonis, M. J., Heidinger, A. K., and Uttal, T.: Daytime global cloud typing from AVHRR and VIIRS: Algorithm description, validation, and comparisons, Journal of Applied Meteorology, 44, 804-826, https://doi.org/10.1175/JAM2236.1, 2005.

Pinto, J. O.: Autumnal mixed-phase cloudy boundary layers in the Arctic, Journal of the Atmospheric Sciences, 55, 2016-2038, https://doi.org/10.1175/1520-0469(1998)055<2016:AMPCBL>2.0.CO;2, 1998.

Pscheidt, I., Senf, F., Heinze, R., Deneke, H., Trömel, S., and Hohenegger, C.: How organized is deep convection over Germany?, Quarterly Journal of the Royal Meteorological Society, 145, 2366-2384, http://dx.doi.org/10.1002/qj.3552, 2019.

Roebeling, R. A., Feijt, A. J., and Stammes, P.: Cloud property retrievals for climate monitoring: Implications of differences between Spinning Enhanced Visible and Infrared Imager (SEVIRI) on METEOSAT-8 and Advanced Very High Resolution Radiometer (AVHRR) on NOAA-17, Journal of Geophysical Research: Atmospheres, 111, https://doi.org/10.1029/2005JD006990, 2006.

Rosenfeld, D. and Woodley, W. L.: Deep convective clouds with sustained supercooled liquid water down to -37.5 °C, Nature, 405, 440-442, https://doi.org/10.1038/35013030, 2000.

Rosenfeld, D., Yu, X., Liu, G., Xu, X., Zhu, Y., Yue, Z., Dai, J., Dong, Z., Dong, Y., and Peng, Y.: Glaciation temperatures of convective clouds ingesting desert dust, air pollution and smoke from forest fires, Geophysical Research Letters, 38, https://doi.org/10.1029/2011GL049423, 2011.

Rybka, H., Burkhardt, U., Köhler, M., Arka, I., Bugliaro, L., Görsdorf, U., Horváth, Á., Meyer, C. I., Reichardt, J., Seifert, A., and Strandgren, J.: The behavior of high-CAPE (convective available potential energy) summer convection in large-domain large-eddy simulations with ICON, Atmos. Chem. Phys., 21, 4285-4318, http://dx.doi.org/10.5194/acp-21-4285-2021, 2021.

Saunders, R., Hocking, J., Turner, E., Rayer, P., Rundle, D., Brunel, P., Vidot, J., Roquet, P., Matricardi, M., Geer, A., Bormann, N., and Lupu, C.: An update on the RTTOV fast radiative transfer model (currently at version 12), Geosci. Model Dev., 11, 2717-2737, http://dx.doi.org/10.5194/gmd-11-2717-2018, 2018.

Schmetz, J., Holmlund, K., Hoffman, J., Strauss, B., Mason, B., Gaertner, V., Koch, A., and Van De Berg, L.: Operational cloud-motion winds from meteosat infrared images, Journal of Applied Meteorology and Climatology, 32, 1206-1225, https://doi.org/10.1175/1520-0450(1993)032<1206:OCMWFM>2.0.CO;2, 1993.

Schmetz, J., Pili, P., Tjemkes, S., Just, D., Kerkmann, J., Rota, S., and Ratier, A.: An introduction to meteosat second generation (MSG), Bulletin of the American Meteorological Society, 83, 977-992, http://dx.doi.org/10.1175/1520-0477(2002)083<0977:AITMSG>2.3.CO;2, 2002.

Seifert, A. and Beheng, K. D.: A two-moment cloud microphysics parameterization for mixed-phase clouds. Part 1: Model description, Meteorology and Atmospheric Physics, 92, 45-66, http://dx.doi.org/10.1007/s00703-005-0112-4, 2006.

Senf, F., Voigt, A., Clerbaux, N., Hünerbein, A., and Deneke, H.: Increasing resolution and resolving convection improve the simulation of cloud-radiative effects over the North Atlantic, Journal of Geophysical Research: Atmospheres, 125, e2020JD032667, https://doi.org/10.1029/2020JD032667, 2020.

Sheffield, A. M., Saleeby, S. M., and van den Heever, S. C.: Aerosol-induced mechanisms for cumulus congestus growth, Journal of Geophysical Research: Atmospheres, 120, 8941-8952, https://doi.org/10.1002/2015JD023743, 2015.

Sotiropoulou, G., Vignon, É., Young, G., Morrison, H., O'Shea, S. J., Lachlan-Cope, T., Berne, A., and Nenes, A.: Secondary ice production in summer clouds over the Antarctic coast: an underappreciated process in atmospheric models, Atmos. Chem. Phys., 21, 755-771, https://doi.org/10.5194/acp-21-755-2021, 2021.

Stengel, M., Kniffka, A., Meirink, J. F., Lockhoff, M., Tan, J., and Hollmann, R.: CLAAS: the CM SAF cloud property data set using SEVIRI, Atmos. Chem. Phys., 14, 4297-4311, http://dx.doi.org/10.5194/acp-14-4297-2014, 2014.

Stephens, G. L.: Radiation profiles in extended water clouds. II: Parameterization schemes, Journal of Atmospheric Sciences, 35, 2123-2132, https://doi.org/10.1175/1520-0469(1978)035<2123:RPIEWC>2.0.CO;2, 1978.

Stith, J. L., Haggerty, J. A., Heymsfield, A., and Grainger, C. A.: Microphysical characteristics of tropical updrafts in clean conditions, Journal of Applied Meteorology, 43, 779-794, https://doi.org/10.1175/2104.1, 2004.

Sullivan, S. C., Barthlott, C., Crosier, J., Zhukov, I., Nenes, A., and Hoose, C.: The effect of secondary ice production parameterization on the simulation of a cold frontal rainband, Atmos. Chem. Phys., 18, 16461-16480, https://doi.org/10.5194/acp-18-16461-2018, 2018.

Takeishi, A. and Storelvmo, T.: A study of enhanced heterogeneous ice nucleation in simulated deep convective clouds observed during DC3, Journal of Geophysical Research: Atmospheres, 123, 13,396-313,420, https://doi.org/10.1029/2018JD028889, 2018.

Taylor, J. W., Choularton, T. W., Blyth, A. M., Liu, Z., Bower, K. N., Crosier, J., Gallagher, M. W., Williams, P. I., Dorsey, J. R., Flynn, M. J., Bennett, L. J., Huang, Y., French, J., Korolev, A., and Brown, P. R. A.: Observations of cloud microphysics and ice formation during COPE, Atmos. Chem. Phys., 16, 799-826, https://doi.org/10.5194/acp-16-799-2016, 2016.

Thomas, J., Barrett, A., and Hoose, C.: Temperature and cloud condensation nuclei (CCN) sensitivity of orographic precipitation enhanced by a mixed-phase seeder–feeder mechanism: a case study for the 2015 Cumbria flood, Atmos. Chem. Phys., 23, 1987-2002, 10.5194/acp-23-1987-2023, 2023.
Twohy, C. H.: Measurements of Saharan dust in convective clouds over the tropical eastern Atlantic ocean, Journal of the Atmospheric Sciences, 72, 75-81, https://doi.org/10.1175/JAS-D-14-0133.1, 2015.
van den Heever, S. C., Carrió, G. G., Cotton, W. R., DeMott, P. J., and Prenni, A. J.: Impacts of nucleating aerosol on Florida storms. Part I: Mesoscale simulations, Journal of the Atmospheric Sciences, 63, 1752-1775, https://doi.org/10.1175/JAS3713.1, 2006.
Vignon, É., Alexander, S. P., DeMott, P. J., Sotiropoulou, G., Gerber, F., Hill, T. C. J., Marchand, R., Nenes, A., and Berne, A.: Challenging and improving the simulation of mid-level mixed-phase clouds over the high-latitude southern ocean, Journal of Geophysical Research: Atmospheres, 126, e2020JD033490, https://doi.org/10.1029/2020JD033490, 2021.
Wan, H., Giorgetta, M. A., Zängl, G., Restelli, M., Majewski, D., Bonaventura, L., Fröhlich, K., Reinert, D., Rípodas, P., Kornblueh, L., and Förstner, J.: The ICON-1.2 hydrostatic atmospheric dynamical core on triangular grids – Part 1: Formulation and performance of the baseline version, Geosci. Model Dev., 6, 735-763, http://dx.doi.org/10.5194/gmd-6-735-2013, 2013.
Zängl, G., Reinert, D., Rípodas, P., and Baldauf, M.: The ICON (ICOsahedral Non-hydrostatic) modelling framework of DWD and MPI-M: Description of the non-hydrostatic dynamical core, Quarterly Journal of the Royal Meteorological Society, 141, 563-579, http://dx.doi.org/10.1002/qj.2378, 2015.
Zhao, B., Wang, Y., Gu, Y., Liou, K.-N., Jiang, J. H., Fan, J., Liu, X., Huang, L., and Yung, Y. L.: Ice nucleation by aerosols from anthropogenic pollution, Nature Geoscience, 12, 602-607, https://doi.org/10.1038/s41561-019-0389-4, 2019.
Zhao, X., Liu, X., Burrows, S. M., and Shi, Y.: Effects of marine organic aerosols as sources of immersion-mode ice-nucleating particles on high-latitude mixed-phase clouds, Atmos. Chem. Phys., 21, 2305-2327, https://doi.org/10.5194/acp-21-2305-2021, 2021.

Tables:

Table 1: Setups of simulations performed in this study.

Num	Experiment	Description
1	$A\times10^{0}$ (CTRL)	Without any perturbations, the CTRL run, used as a reference.
2	$A\times10^{-2}$	INP concentrations for both immersion and deposition mode are scaled by multiplying parameter A in Equation (1) by 10^{-2}.
3	$A\times10^{-1}$	Same as num. 2, but multiplying by 10^{-1}.
4	$A\times10^{1}$	Same as num. 2, but multiplying by 10^{1}.
5	$A\times10^{2}$	Same as num. 2, but multiplying by 10^{2}.
6	$A\times10^{3}$	Same as num. 2, but multiplying by 10^{3}.
7	$A\times10^{0}$_NSIP	INP concentration as in CTRL. The secondary ice production (rime-splintering process) is switched off.
8	DEC05	Initial and lateral temperature decreases from 3 to 12 km with a maximum increment of 5 K. No perturbations in INPs ($A\times10^{0}$).
9	DEC03	Same as num. 8, but with a maximum increment of 3 K.
10	INC03	Initial and lateral temperature increases from 3 to 12 km with a maximum increment of 3 K. No perturbations in INPs ($A\times10^{0}$).
11	INC05	Same as num. 10, but with a maximum increment of 5 K.

Figures:

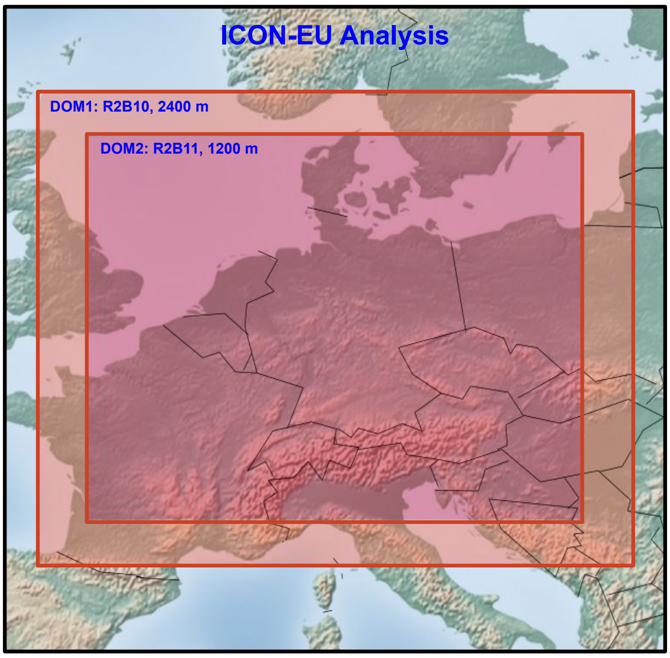

Figure 1: The simulation domains.

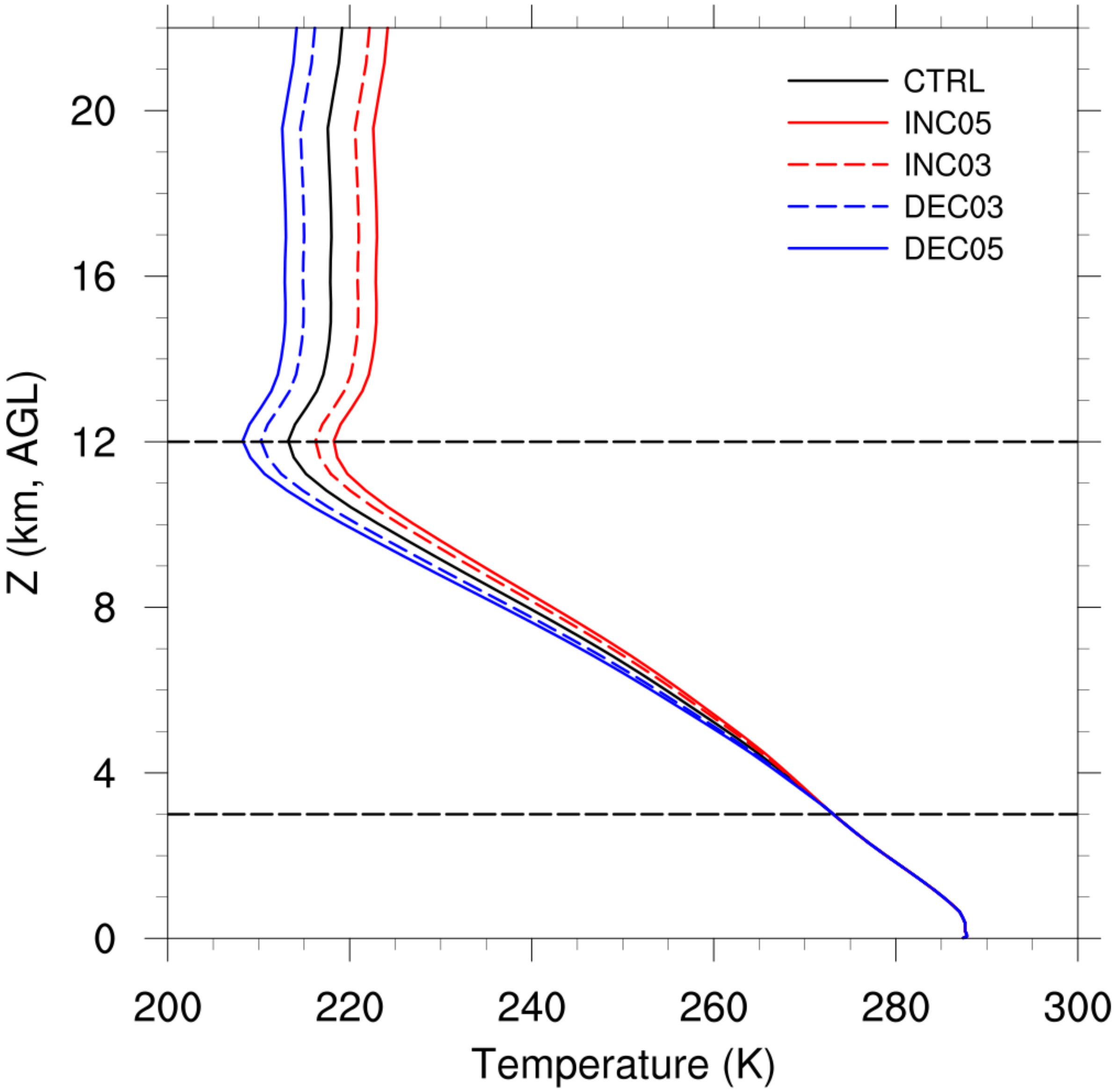

Figure 2: Domain averaged initial temperature profiles. The same modification was applied to the lateral boundary conditions.

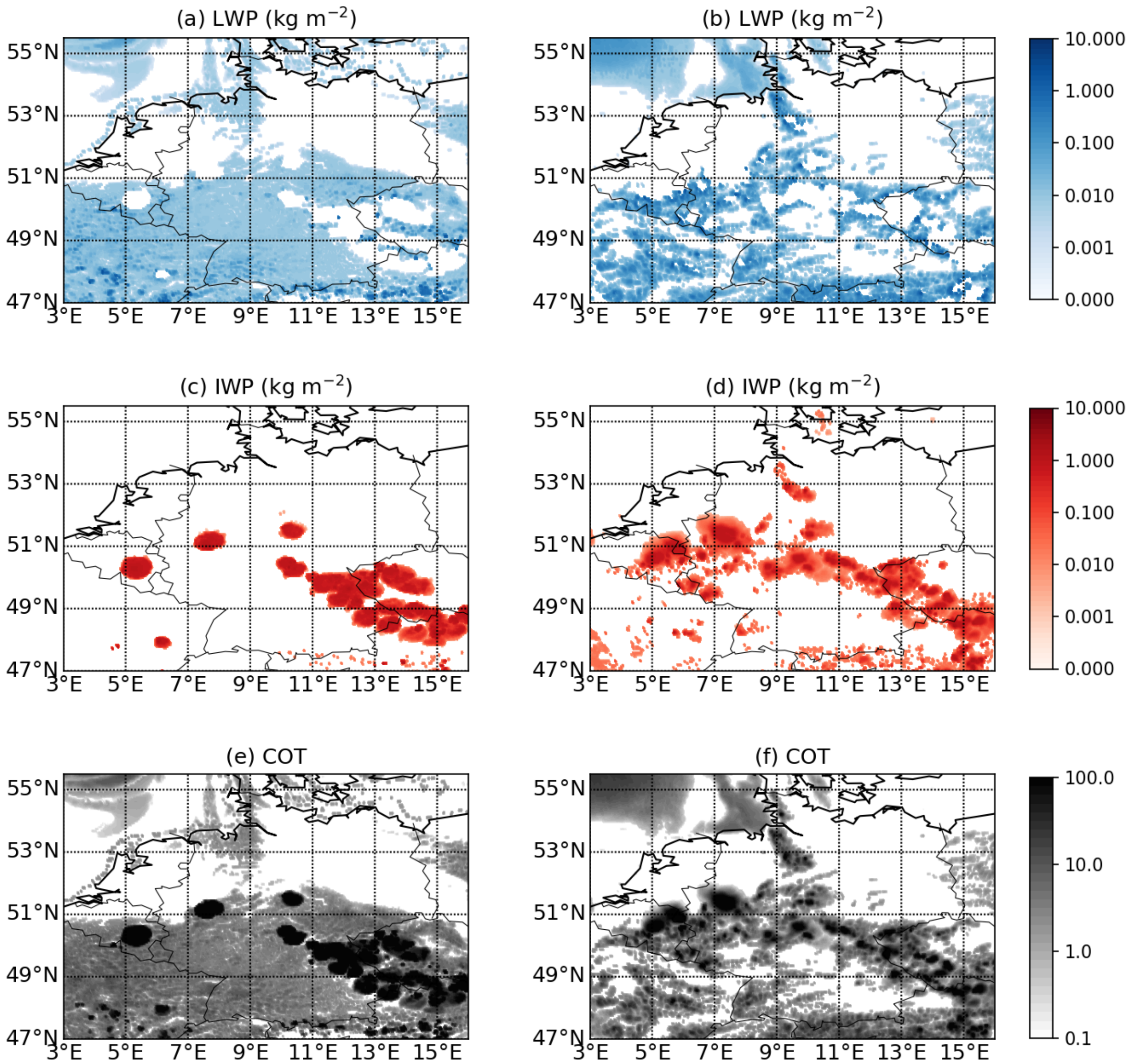

Figure 3: Spatial distributions of retrieved cloud liquid water path (LWP), ice water path (IWP), and cloud optical thickness (COT) at 13:00 UTC. The left panel is for the CTRL case (a, c, e) and the right panel is for the CLAAS-2 product (b, d, f).

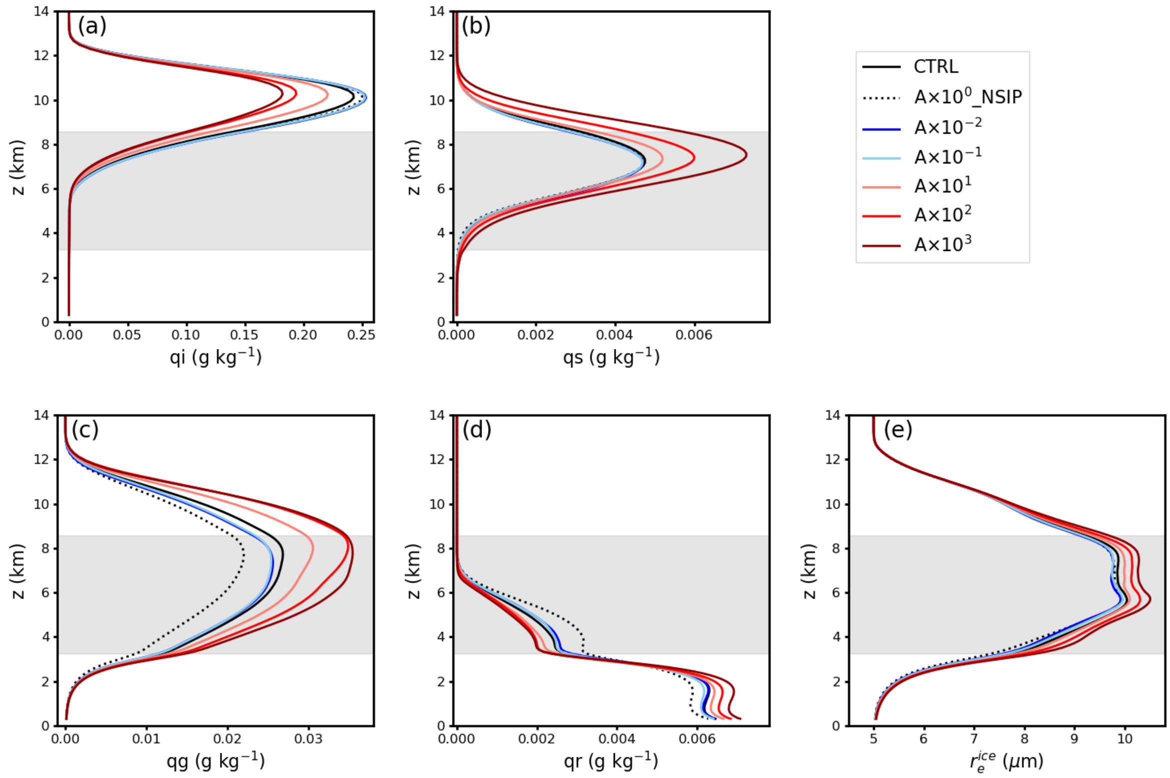

Figure 4: Spatial- and time-averaged (9:00~19:00) profiles of cloud mass mixing ratios of (a) ice crystals, (b) snow, (c) graupel, (d) rainwater, and (e) ice crystal effective radius. Mass mixing ratio unit is g kg^{-1} and the unit of ice crystal effective radius is μm. Shaded area indicates the spatial- and time-averaged mixed-phase region.

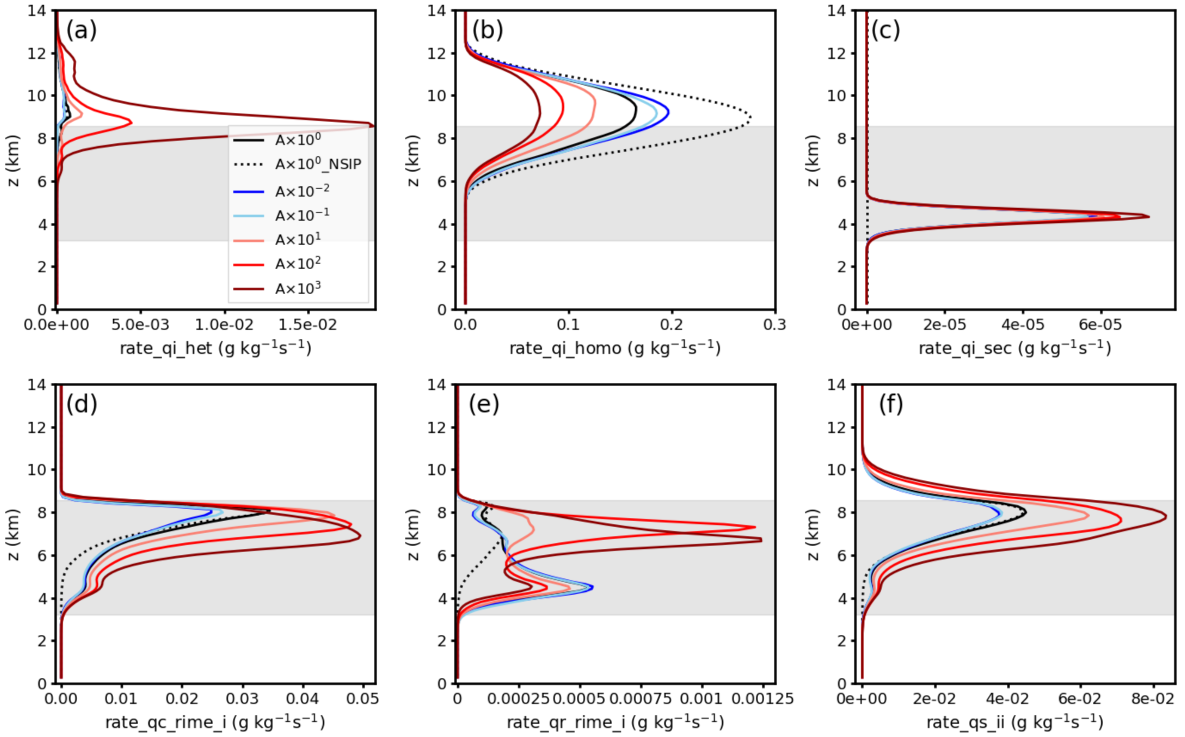

Figure 5: Spatial- and time-averaged (9:00~19:00) profiles of process rates of (a) heterogeneous freezing (immersion and deposition nucleation), (b) homogeneous freezing, (c) secondary-ice production (rime-splintering), (d) cloud droplets rimed with ice crystals, (e) rain droplets rimed with ice crystals, (f) collection between ice and ice. Unit is g kg-1 s-1. The average mixed-phase layer (0~-38 °C) is roughly in between 3.2 and 8.6 km. Shaded area indicates the spatial- and time-averaged mixed-phase region. Unit is g kg^{-1}s^{-1}.

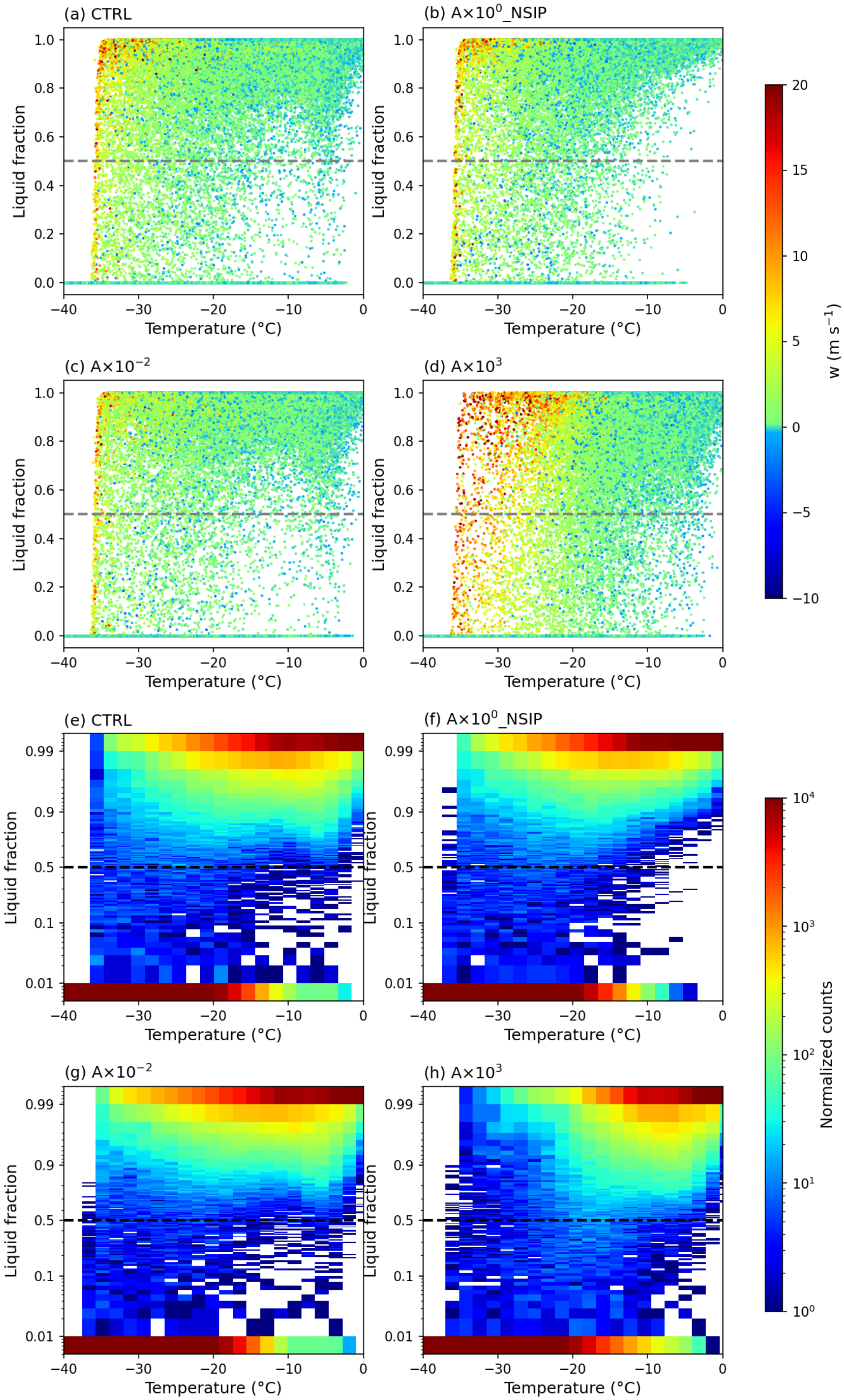
(a) CTRL
(b) A×10^0_NSIP
(c) A×10^{-2}
(d) A×10^3
(e) CTRL
(f) A×10^0_NSIP
(g) A×10^{-2}
(h) A×10^3
Liquid fraction
Temperature (°C)
w (m s^{-1})
Normalized counts

1035

Figure 6: In-cloud supercooled liquid mass fraction distribution as a function of temperature (binned by 1°C) between 9:00 and 19:00 (a-d) for the 4 cases (A$\times10^0$, A$\times10^0$_NSIP, A$\times10^{-2}$, A$\times10^3$), the colour of points indicates the vertical wind velocity (unit, m s^{-1}). 2-D histogram of in-cloud liquid mass fraction versus temperature (e-f).

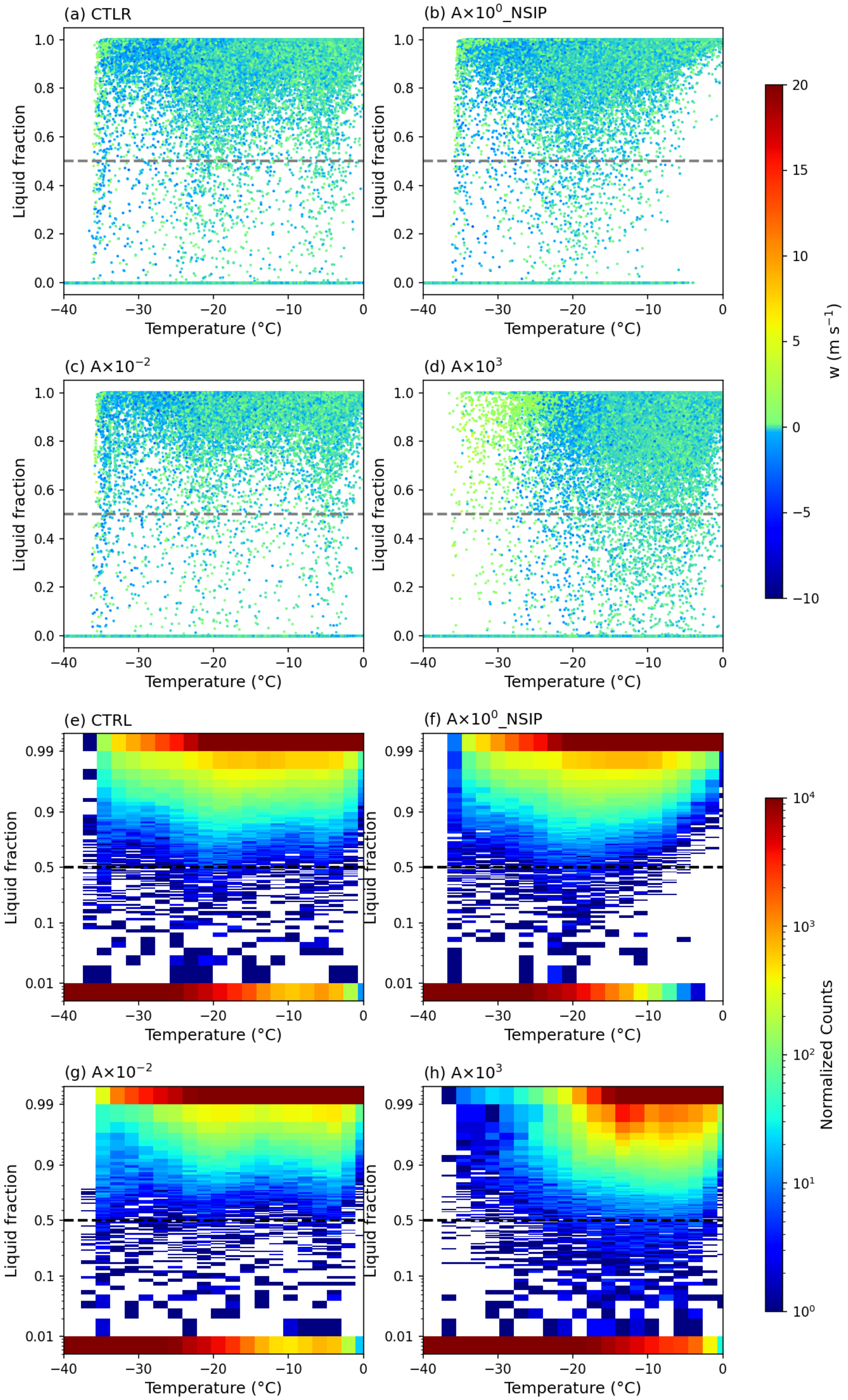
(a) CTLR
(b) A×10⁰_NSIP
(c) A×10⁻²
(d) A×10³
(e) CTRL
(f) A×10⁰_NSIP
(g) A×10⁻²
(h) A×10³
Liquid fraction
Temperature (°C)
w (m s⁻¹)
Normalized Counts

Figure 7: Cloud-top supercooled liquid mass fraction distribution as a function of temperature (binned by 1°C) between 9:00 and 19:00 (a-d) for the 4 cases ($A\times10^0$, $A\times10^0$_NSIP, $A\times10^{-2}$, $A\times10^3$), the colour of points indicates the vertical wind velocity (unit, m s^{-1}). 2-D histogram of cloud-top liquid mass fraction versus temperature (e-f).

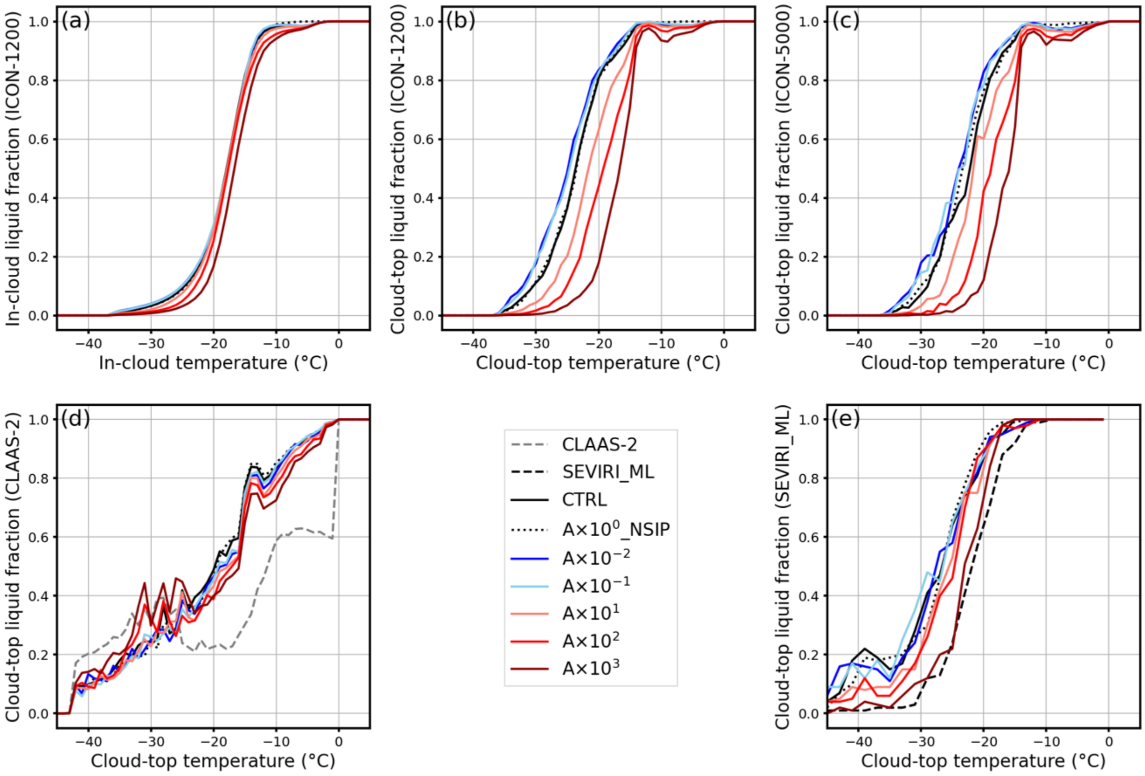

Figure 8: Liquid cloud pixel fraction as a function of temperature from 9:00 to 19:00 UTC for the INP sensitivity experiments, (a) in-cloud fraction calculated from simulations on ICON native grid (~1200 m), (b) cloud-top fraction calculated from simulations on ICON native grid (~1200 m), (c) cloud-top fraction calculated from simulations on SEVIRI's grid (~5000 m), (d) cloud-top fraction calculated by remote-sensing retrieval algorithms to produce CLAAS-2 dataset, and (e) cloud-top fraction calculated by remote-sensing retrieval software suite SEVIRI_ML. The temperature is binned by 1°C in (a), (b), (c), and (d), and by 2°C in (e).

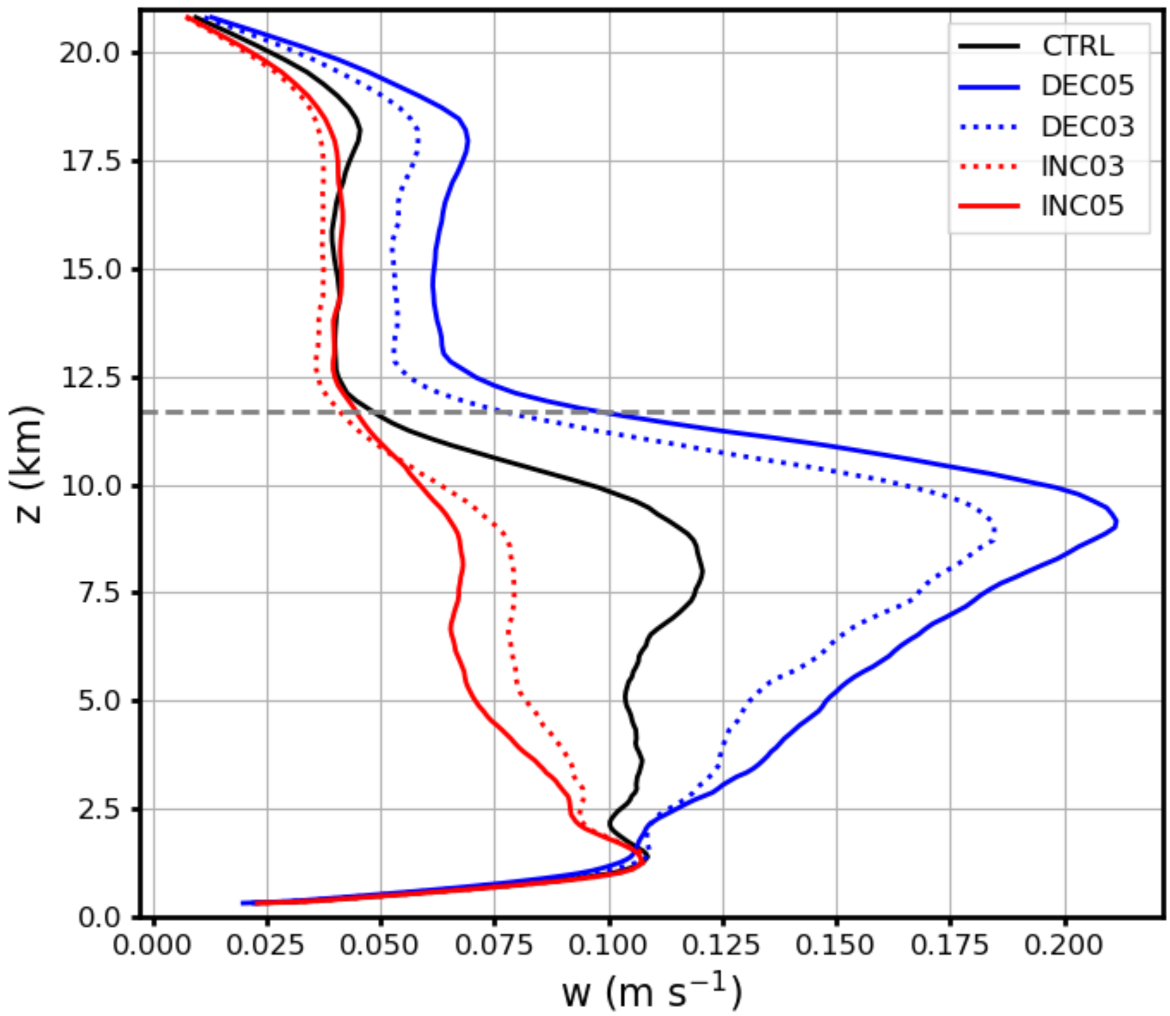

Figure 9: Spatial- and time-averaged (9:00~19:00) profiles of vertical velocities (w values ≤ 0 m s^{-1} are excluded). The dashed grey line indicates the clout top height which is about 11.7 km.

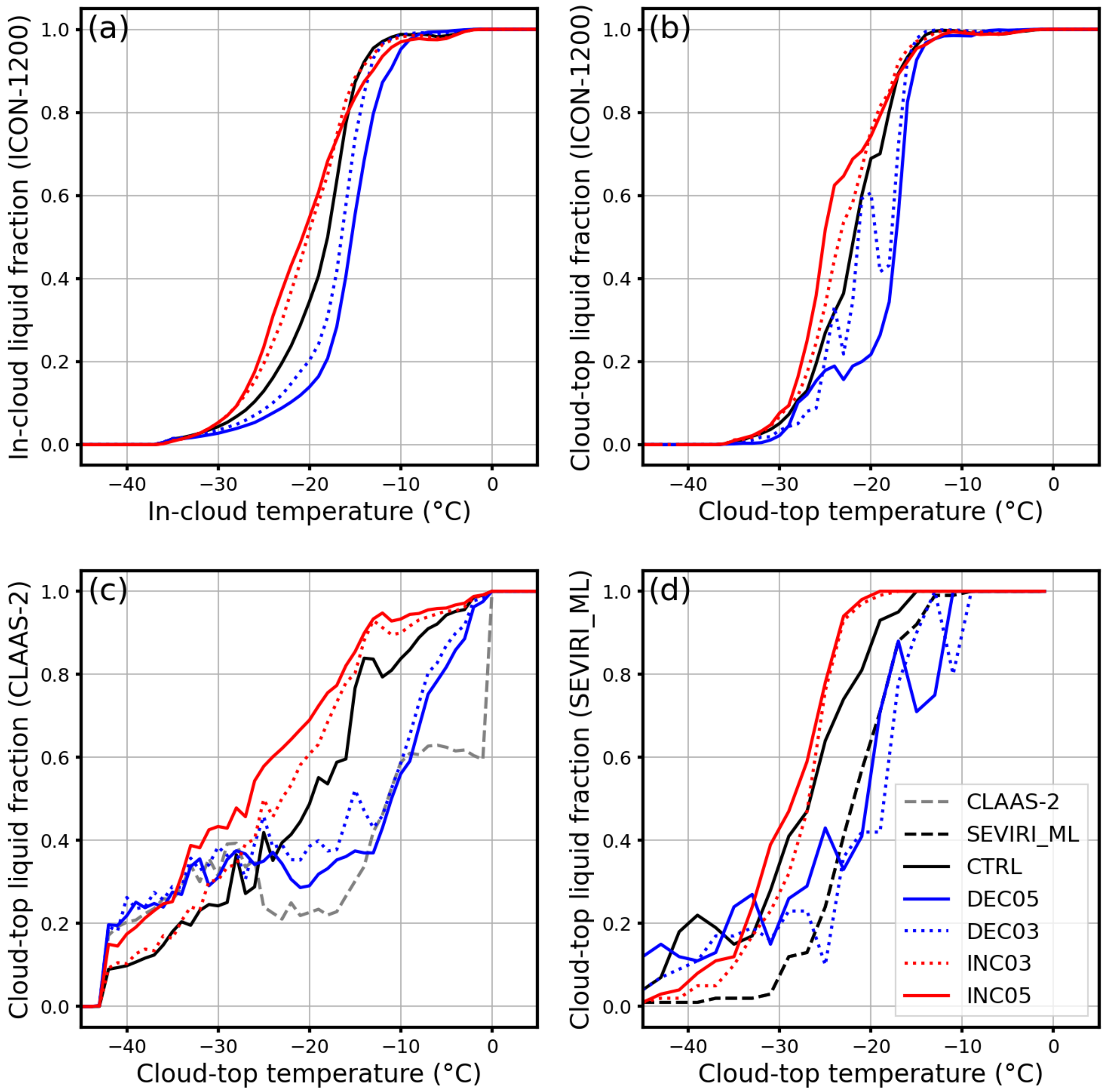

Figure 10: Liquid cloud pixel fraction as a function of temperature from 9:00 to 19:00 for the thermodynamic sensitivity experiments, (a) in-cloud fraction calculated directly from simulations, (b) cloud-top fraction calculated from directly simulations, (c) cloud-top fraction calculated by remote-sensing retrieval algorithms to produce CLAAS-2 dataset, and (d) cloud-top fraction calculated by remote-sensing retrieval software suite SEVIRI_ML. The temperature is binned by 1°C in (a), (b), and (c), and by 2°C in (d).

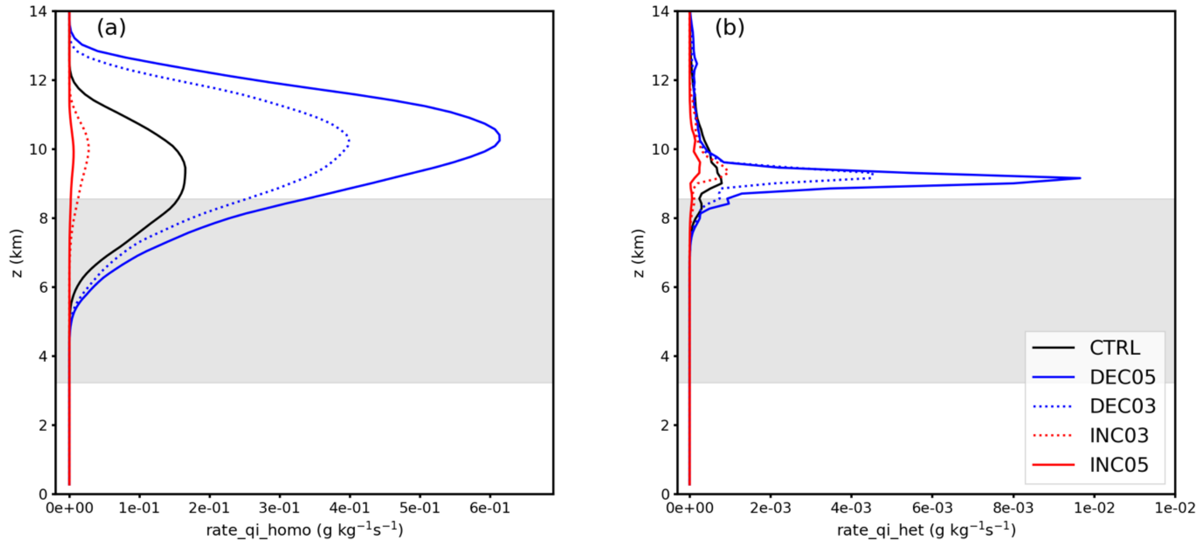

Figure 11: Spatial- and time-averaged (9:00~19:00) profiles of process rates of (a) homogeneous freezing, (b) heterogeneous freezing (immersion and deposition nucleation) for cases with perturbed initial thermodynamic states. Shaded area indicates the spatial and time-averaged mixed-phase region. Unit is g kg^{-1} s$^{-1.}$